Study of the ATLAS MDT Spectrometer using High Energy CERN combined Test beam Data

C. Adorisio [f], G. Aielli [k], Th. Alexopoulos [r], M. Alviggi [h],
C. Amelung [b], Ch. Anastopoulos [ah], G. Avolio [f,5],
R. Avramidou [m,5], K. Bachas [ah], P. Bagnaia [j], R. Ball [m],
M. Barisonzi [o], A. Baroncelli [ℓ], M. Barone [c], F. Bauer [v,1],
M. Bellomo [i], Y. Benhammou [z], J. Bensinger [a], M. Beretta [c],
R.M. Bianchi [ℓ,6], M. Bianco [g], C. Bini [j], G. Bobbink [o],
A. Borisov [u], H. Boterenbrood [o], I. Boyko [d], P. Branchini [ℓ],
E. Brambilla [g], G. Brandenburg [ad], U. Bratzler [aa], S. Bressler [y],
G. Brouwer [o], M. Cambiaghi [i], V. Canale [h], M. Caprio [h],
R. Cardarelli [k], F. Cerutti [b,7], J. W. Chapman [m], G. Chelkov [d],
L. Chevalier [v], G. Chiodini [g], M. Cirilli [b,9], R. Coco [af],
M. Curatolo [c], T. Dai [m], R. De Asmundis [h], D. Dedovich [d],
M. Della Pietra [h], D. Della Volpe [h], G. DeZorzi [j],
A. Di Ciaccio [k], A. DiDomenico [j], S. Di Luise [ℓ], A. Di Simone [k],
M. Dris [r], A. Dushkin [a], J. Ernwein [v], B. Esposito [c], E. Etzion [z],
R. Fakhrutdinov [u], S. Falciano [j], D. Fassouliotis [s], R. Ferrari [i],
A. Formica [v], C.Fukunaga [aa], G. Gaudio [i], Ev. Gazis [r],
P.-F. Giraud [v], E. Gorini [g], F. Grancagnolo [g], J. A. Gregory [m],
H. Groenstege [o], J. Guimaraes da Costa [ad], C. Guyot [v],
A. Harel [y], R. Hart [o], K. Hashemi [a], S. Hassani [v], G. Herten [ac],
S. Horvat [n], P. Hurst [ad], R. Ichimiya [q], P. Iengo [h], M. Ikeno [p],
P. Ioannou [s], M. Iodice [ℓ], M. Ishino [e], H. Iwasaki [p], Y. Kataoka [e],
A. Khodinov [ag], A. Konig [ai], O. Kortner [n], S. Kotov [n],
C. Kourkoumelis [s], A. Kozhin [u], A. Krepouri [ah], H. Kroha [n],
Z. Krumshteyn [d], H. Kurashige [q], U. Landgraf [ac], F. Lacava [j],
E. Lançon [v], A. Lanza [i], J.-F. Laporte [v], D. Lellouch [ab],
D. S. Levin [m], L. Levinson [ab], B. Liberti [k], R. Lifshitz [y],
F. Linde [o], C. Luci [j], N. Lupu [y], G. Maccarrone [c], T. Maeno [b],
K. Mair [b], S. Maltezos [r], A. Manz [n], M. Marchesotti [b,11],

E. Meoni [f], G. Mikenberg [ab], W. Mohr [ac], S. Mohrdieck-Moeck [n],
K. Nagano [p], R. Nicolaidou [v,2], K. Nikolaev [d], K. Nikolopoulos [s],
A. Nisati [j], H. Nomoto [e], J. Oliver [ad], D. Orestano [ℓ],
L. S. Osborne [af], A. Ouraou [v], S. Palestini [b], E. Pasqualucci [j],
A. Passeri [ℓ], F. Pastore [j], S. Patricelli [h], R. Perrino [g],
Ch. Petridou [ah], F. Petrucci [ℓ,3], S. Podkladkin [g], A. Policicchio [f],
D. Pomarede [v], P. Ponsot [v], L. Pontecorvo [j], M. Primavera [g],
D. Rebuzzi [i,10], R. Richter [n], A. Rimoldi [i], S. Rosati [b,4,8],
J. Rothberg [w], H. Sakamoto [e], D. Salvatore [f], D. Sampsonidis [ah],
R. Santonico [k], O. Sasaki [p], A. Schricker [a], S. Schuh [b],
P. Schune [v], M. Shoa [ab], N. Skvorodnev [a], K. Sliwa [x],
E. Solfaroli Camillocci [k,8], S. Spagnolo [g], L. Spogli [ℓ],
E. Strauss [ag], Y. Sugaya [t], S. Tanaka [p], S. Tarem [y],
F. E. Taylor [af], S. Todorova [x], I. Trigger [b,12], I. Tsiafis [ah],
G. Tsipolitis [r], Ch. Valderanis [ah], P. Valente [j], W. Vandelli [i,5],
H. van der Graaf [o], R. Vari [j], S. Veneziano [j], A. Ventura [g],
S. Ventura [c], J. Vermeulen [o], S. Vlachos [r], M. Vreeswijk [o],
Y. Yasu [p], H. Wellenstein [a], P. Werneke [o], T. Wijnen [ai],
M. Wolter [x], J. Wotschack [b], M. Woudstra [ae], F. Zema [f,5],
Z. Zhao [m], A. Zhemchugov [d], B. Zhou [m], S. Zimmerman [ac]

[a] *Brandeis University, Mailstop 057, 415 South Street, Waltham, MA 02454, USA*
[b] *CERN, CH-1211 Genève 23, Switzerland*
[c] *INFN Laboratori Nazionali di Frascati, via Fermi, 40, I-00044, Frascati, Italy*
[d] *Joint Inst. for Nuclear Research (JINR), 141980, Dubna, Moscow Region, Russia*
[e] *ICEPP, University of Tokyo, 7-3-1 Hongo, Bunkyo-ku, Tokyo 113-8654, Japan*
[f] *Università della Calabria and INFN, Cosenza, p. Bucci, I-87036 Arcavacata di Rende (Cosenza), Italy*
[g] *Università del Salento and INFN, Lecce, via Arnesano, 73100 Lecce, Italy*
[h] *Università di Napoli "Federico II" and INFN, Napoli, via Cintia, I-80126, Napoli, Italy*
[i] *Università di Pavia and INFN, Pavia, via Bassi, 6, I-27100, Pavia, Italy*
[j] *Università di Roma La Sapienza and INFN, Roma, p.le Moro 2, I-00185, Roma, Italy*
[k] *Università di Roma Tor Vergata and INFN, Roma 2, v. Ricerca Scientifica 1, I-00133, Roma, Italy*

[ℓ]*Università di Roma Tre and INFN, Roma Tre, via della Vasca Navale, 84, I-00146, Roma, Italy*

[m]*Michigan University, Ann Arbor, MI 48109, USA*

[n]*Max-Planck-Institut für Physik, Föhringer Ring 6, 80805 München, Germany*

[o]*Nikhef National Institute for Subatomic Physics, and University of Amsterdam, Kruislaan 409, P.O. Box 41882, NL-1009 DB Amsterdam, The Netherlands*

[p]*High Energy Accelerator Res. Organ. (KEK), 1-1 Oho, Tsukuba, Ibaraki 305-0801 Japan*

[q]*Kobe University, 1-1 Rokkodai-cho, Nada-ku, Kobe 657-8501 Japan*

[r]*National Technical University Athens, Zografou Campus, GR-157, 80 Zografou, Greece*

[s]*University of Athens, 15701 Ilissia, Greece*

[t]*Research Center for Nuclear Physics, Osaka University, Osaka, Japan*

[u]*Institute for High Energy Physics (IHEP), Pobeda str. 1, 142281, Protvino, Moscow Region, Russia*

[v]*Dapnia, CEA - Saclay, F-91191 Gif sur Yvette Cedex, France*

[w]*University of Washington, 3910 15th Ave. NE, Seattle, WA 98195-1560, USA*

[x]*Tufts University, Medford, MA 02155, USA*

[y]*Technion - Israel Institute of Technology, Haifa 32000, Israel*

[z]*Tel Aviv University, P.O. Box 39040, Tel Aviv 69978, Israel*

[aa]*Tokyo Metropolitan University, 1-1 Minami-Osawa, Hachioji-shi Tokyo, 192-0397 Japan*

[ab]*Weizmann Institute of Science, P.O. Box 26, Rehovot 76100, Israel*

[ac]*University of Freiburg, Fakultät für Physik, Hermann-Herder-Str. 3, 79104 Freiburg i. Br., Germany*

[ad]*Harvard University, LPPC, 18 Hammond Street Cambridge, MA 02138, USA*

[ae]*Univ. of Massachusetts, Department of Physics 1126 Lederle Graduate Research Tower (LGRT) Amherst, MA 01003-9337 USA*

[af]*Massachusetts Institute of Technology, LNS, 77 Massachusetts Avenue, Cambridge, MA 02139-4307, USA*

[ag]*Physics and Astronomy, SUNY, Stony Brook, NY 11794-3800, USA*

[ah]*Department of Physics, Aristotle University of Thessaloniki, 54124, Thessaloniki, Greece*

[ai]*Radboud University Nijmegen/Nikhef, Dept. of Exp. High Energy Physics, Toernooiveld 1, NL - 6525 ED Nijmegen , The Netherlands*

3

Abstract

In 2004, a combined system test was performed in the H8 beam line at the CERN SPS with a setup reproducing the geometry of sectors of the ATLAS Muon Spectrometer, formed by three stations of Monitored Drift Tubes (MDT). The full ATLAS analysis chain was used to obtain the results presented in this paper. The basic design performances of the Muon Spectrometer were verified. The stability of MDT calibration constants, the alignment system using optical devices and high energy tracks, as well as the intrinsic sagitta resolution of the Muon Spectrometer were studied and found to agree with expectations. The reconstruction of muon tracks using the combined information from both the Inner Detector and the Muon Spectrometer are also presented.

[1] Corresponding author. *E-mail address* : Florian@hep.saclay.cea.fr

[2] Corresponding author. *E-mail address* : Rosy.Nicolaidou@cern.ch

[3] Corresponding author. *E-mail address* : petrucci@roma3.infn.it

[4] Corresponding author. *E-mail address* : Stefano.Rosati@roma1.infn.it

[5] Now at CERN, CH-1211 Genève 23, Switzerland

[6] Now at University of Freiburg, Fakultät für Physik, Hermann-Herder-Str. 3, 79104 Freiburg i. Br., Germany

[7] Now at INFN Laboratori Nazionali di Frascati, via Fermi, 40, I-00044, Frascati, Italy

[8] Now at Università di Roma La Sapienza and INFN, Roma, p.le Moro 2, I-00185, Roma, Italy

[9] Now at Michigan University, Ann Arbor, MI 48109, USA

[10] Now at Max-Planck-Institut für Physik, Föhringer Ring 6, 80805 München, Germany

[11] Now at Università di Pavia and INFN, Pavia, via Bassi, 6, I-27100, Pavia, Italy

[12] Now at TRIUMF, 4004 Wesbrook Mall, Vancouver, BC, V6T 2A3 Canada.

1 Introduction

The Muon Spectrometer [1] of the ATLAS detector was designed to provide a stand-alone trigger for muons with transverse momentum of several GeV/c as well as a measurement of final state muons with a momentum resolution of about 3% over most of the momentum range. Tracking in the Muon Spectrometer is based on the magnetic deflection of muon tracks in large superconducting air-core toroid magnets. Over the range $|\eta| \leq 1.0$, magnetic bending is provided by the large barrel toroid which provides a field integral $\int Bdl$ between 2 and 6 Tm. For $1.4 \leq |\eta| \leq 2.7$ muon tracks are bent by two smaller end-cap toroid magnets contributing between 4 and 8 Tm. The bending in the region $1.0 \leq |\eta| \leq 1.4$, usually referred to as the transition region, is provided by a combination of barrel and end-cap fields.

The Muon Spectrometer is a 4π detector, which consists of four detector technologies. Over most of the spectrometer acceptance, Monitored Drift Tube (MDT) chambers are used for the precision measurement of muon tracks with Cathode Strip chambers (CSC) deployed in the high rapidity region ($2.0 \leq |\eta| \leq 2.7$) of the first detection layer of each end-cap. The MDTs are made of gas filled aluminum tubes with a central wire and measure charged particle tracks with an average spatial resolution of 80 μm. Resistive Plate Chambers (RPC) provide the trigger for muons in the barrel region, whereas Thin Gap Chambers (TGC) serve the same purpose in the higher background region of the end-cap. The signals from the trigger chambers are digitized on the detector and sent to ASIC-based coincidence matrix boards. These boards perform the functions needed for the trigger algorithms and apply p_T cuts according to preset thresholds. The trigger chambers are also used to provide the coordinate along the drift tubes (the second coordinate), which is not measured by MDT chambers.

The determination of the muon momentum is based on the measurement of three points along the track of the particle deflected in the magnetic field. Each of the three stations [13] in the muon system provides one measurement point along the track. It is convenient to express the curvature in terms of the sagitta, which is the distance from the point measured in the middle station to the straight line connecting the points in the inner and outer stations. The precision of the sagitta measurement is a direct measure of the precision of the muon momentum.

A muon of momentum 1 TeV/c has a sagitta of about 500 μm in the bar-

---

[13] An ATLAS muon station is made of 6 to 8 layer of Monitored Drift Tubes (MDT) for precision measurements, which in addition can be equipped with trigger chambers: Resistive Plate Chambers (RPC) in the barrel, Thin Gap Chambers (TGC) in the end-cap. The MDTs (and CSCs) provide a number of hits reconstructed as a segment.

rel. The target momentum measurement precision of $\Delta p_T/p_T = 10\%$ requires a sagitta precision of 50 μm. The actual precision depends not only on the local precision of the points measured in the muon chambers, but also on the relative positions of the three stations. These positions need therefore to be known with an accuracy that is comparable to the individual chamber point measurement precision. The total contribution of the chamber point measurements to the sagitta precision should be less than 40 μm. Permanently active alignment systems are needed to continuously monitor the chamber positions and deformations with the needed accuracy.

The reconstruction of muon tracks is also affected by the accuracy of the relation between drift times and impact radii in the tubes ($r(t)$ in the following). A 30 μm uncertainty in the knowledge of this relation combined with an average single-wire resolution of 80 μm has an effect on the momentum resolution for $\eta \leq 1.4$ (the *barrel* region) which varies between 1% and 10% for muon momenta in the range 100 to 1000 GeV/c. For $\eta > 1.4$ (the *end-cap* region) the effect on momentum resolution varies between 1% and 6% for the same muon momenta range.

A large test stand of ATLAS detectors, including all the Muon Spectrometer components was operated at CERN in the H8 beam line from 2000 to 2004. A detailed description of the system test performed at the H8 beam line during 2003 can be found in [2]. The setup exposed to the beam represented about 1 % of the ATLAS detector including two sectors of the Muon Spectrometer for both the barrel and the end-cap, Inner Tracking detectors [3], modules of the hadronic calorimeter [4] and of the electromagnetic Liquid Argon calorimeter [5]. Large samples of events were collected with various operating conditions and layouts. Data were taken either independently with the various subdetectors (non-combined runs) or using the same trigger and DAQ (combined runs). A particle beam of momentum up to 350 GeV/c from the SPS accelerator was used to study various aspects of the spectrometer. In this paper the performance of the muon system and its components during the 2004 H8 test period is reported. The results are based on tools and analysis that are reported in detail in the following references [6],[7],[8],[9] and [10].

2   The experimental setup

The setup of the 2004 ATLAS System Test consists of four parts: the Inner Detector, the Calorimeters, the Muon Detectors and the beam line elements. In the *Combined Test Beam* (CTB), the Inner Detector consisted of three layers of silicon pixel modules, four layers of two silicon strip detectors (SCT) and two wedges of the straw drift tube detector (TRT). The Liquid Argon (LAr) electromagnetic calorimeter module and the hadronic calorimeter (TileCal) modules were both placed on a table which could be rotated and translated

to expose specific cells to the beam. The dump between H8A and H8B was a 3.2 m long block of iron along the beam direction with a transverse area of 800 mm^2. It was kept in place for most of the data taking. A detailed description of the setup can be found in [2].

The H8 muon stand, as shown in Fig. 1, consists of two parts, a barrel stand and an end-cap stand. The barrel setup reproduced one ATLAS barrel sector with its MDT [11] and RPC [12] stations. It consisted of six MDT chambers, two of each type: inner (BIL), middle (BML) and outer (BOL) chambers, fully instrumented with Front End electronics (FE) [13] read out with a Muon Readout Driver (MROD) [14] and fully equipped with an optical alignment system. Each MDT triplet (BIL, BML, BOL) formed an ATLAS-like tower. Tubes of the barrel sector are vertical. In the barrel setup there were six RPC doublets: four middle chambers (BML) and two outer chambers (BOL).

In the end-cap stand, which reproduced a muon spectrometer end-cap sector, there were 6 MDT chambers (Small and Large): two inner (EI), two middle (EM) and two outer (EO). As in the barrel they were fully instrumented with FE and read out through one MROD. The chambers were equipped with calibrated sensors for absolute alignment. Two alignment bars, discussed in section 3.2.3, were part of each End Cap station, in order to perform a test of all functionalities of the alignment system. For triggering in the end-cap, there were three TGC units [15] : one triplet and two doublets fully instrumented with on-chamber electronics.

Two additional muon stations were installed in the test stand. One inner station (called $BILrot$ in the following) was placed on a remotely operated rotating support. The support allowed the rotation of the chamber of up to ± 15 degrees around the vertical axis of the chamber which made it possible
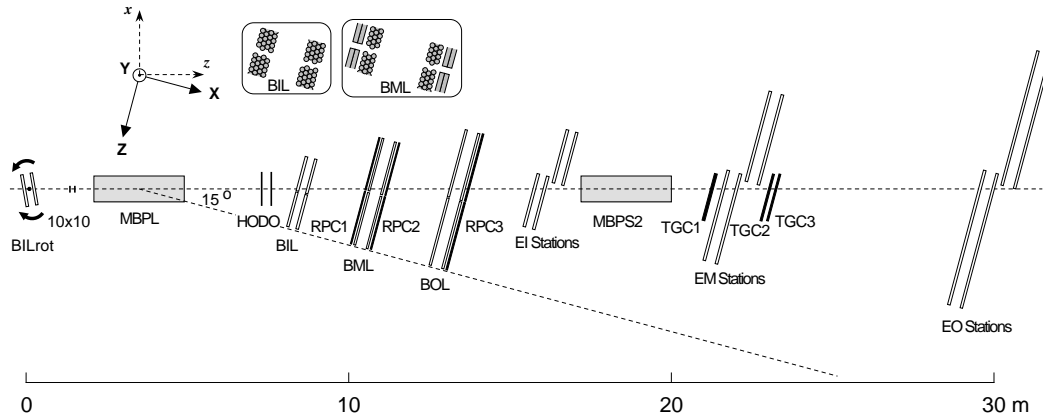

Fig. 1. Schematic view of the 2004 test beam setup in the H8 area. From left to right: the BIL rotating chamber, 10 x 10 trigger, the MBPL bending magnet, the hodoscope trigger, the barrel BIL, BML, BOL stations equipped with the trigger RPC, the end-cap EI stations, the MBPS2 bending magnet, the first TGC trigger chamber, the end-cap EM stations, the other two TGC chambers and and the end-cap EO stations. The coordinates in capital letters are used by the alignment system; the ones in small letters are used by the offline reconstruction software.

to enlarge the angular range of muon tracks for the calculation of the space versus time relation ($r(t)$ in the following). One inner station (BIS) was placed in front of the Liquid Argon Calorimeter to measure accurately the particle trajectory at the entrance of the calorimeter, in order to study in detail the response of the calorimeter for different impact points within the electrode structure.

Three bending magnets, namely MBPSID, MBPL, and MBPS2, were used during different periods. Both the pixel and the SCT detectors were located inside the magnetic field of the MBPSID magnet not shown in Fig. 1, whereas the TRT was installed outside the magnet. The orientation of the field was horizontal to deflect particles vertically, a geometry which emulates the layout in ATLAS. The MBPL magnet was installed in front of the muon barrel stand and was used to bend tracks horizontally, in the plane perpendicular to the MDT tubes, in order to move the beam spot over the muon chambers, emulating tracks of different polar angle, and allowing a more complete validation of the system. This magnet was operated with various currents and both polarities. Finally, the MBPS2 magnet was installed between the EI and the EM stations of the end-cap muon stand for muon momentum measurements.

Two coordinate systems are used throughout this paper and are identified by capital and small letters as shown in Fig. 1. In the first one (used by the alignment system), the X-axis is along the H8-beam, the Z-axis is horizontal and the Y-axis is vertical to form an orthogonal reference frame. In the second one (used by the offline reconstruction software), the z-axis is along the H8-beam and the x-axis is horizontal. The origins of the systems (perigee) are on the axis of the H8 beam-line, at the entrance surface of the Inner Detector magnet (MBPSID). It was chosen as similar as possible to the ATLAS reference system for the barrel stand.

Two trigger systems were available: a small area trigger given by the coincidence of two (10 x 10) cm^2 scintillators centered on the beam line and a large area trigger of (60 x 100) cm^2, called hodoscope trigger, given by the coincidence of the signals from two planes of six scintillator slabs of (10 x 100) cm^2 each and the small area trigger in negative logic.

The monitoring of the parameters of the detectors working conditions was realised via the Detector Control System (DCS) [16]. This included the settings of the programmable parameters of the front-end electronics and the monitoring of the environmental parameters. The discriminator threshold was set between 34 and 52 mV in different runs. The nominal discriminator threshold of 40 mV corresponded to about 16 primary electrons. In particular the temperature of each chamber was measured at regular time intervals at several locations by means of temperature probes. The measurements were recorded in the *Conditions Data Base*.

The MDT gas mixture was the nominal [17] $Ar(93\%)$ and $CO_2(7\%)$ at 3 *bar* absolute pressure. The gas gain was set to $2 \cdot 10^4$.

3 Data analysis

Data samples corresponding to different operating conditions were taken with the muon system only (non-combined runs) during summer 2004, and later during fall together with the Tile and LAr calorimeters (combined runs). In the runs taken with the (10 x 10) cm^2 trigger, the beam spot illuminates three tubes and was observed to be stable, from summer to fall, within approximately one tube width. For some runs, a scan of beam momentum was performed between 100 and 250 GeV/c, by varying the settings of the H8 beam-line. These nominal values refer to the beam momentum at the H8 entrance, before the calorimeters and the beam dump. Alignment studies related to controlled movements of the MDT chambers were performed with runs from both data taking periods. The data from summer were used for testing the alignment with tracks and for determining the efficiency of MDTs for various beam momenta and signal thresholds. The effect of placing material in front of a barrel MDT was studied with the fall data.

3.1 Calibration procedures

A sequence of calibrations have to be performed to reconstruct tracks from raw MDT data (i.e. tube identifiers and TDC information). The first step is the determination of the t_0 for each tube defined as the drift time associated to a particle crossing the tube at a distance r=0 from the wire and representing a relative delay between different channels. This value has to be subtracted from the time measurements. t_0 is computed using a fit procedure to the drift time distributions which yields also other parameters of the drift time distribution such as the maximum drift time t_1. This first procedure does not require any track reconstruction. Drift times are expressed in units of TDC counts, one TDC count corresponding to 25 $ns/32 = 0.78125$ ns. The drift time distribution of each MDT tube is fitted with an analytic function which consists of two distinct Fermi Dirac functions describing the leading edge, the trailing edge and an exponential function for the central part. The analytic expression of the function is given below:

$$f(t) = p_1 + \frac{p_2 \left(1 + p_3 e^{-\frac{t-p_5}{p_4}}\right)}{\left(1 + e^{-\frac{t-p_5}{p_7}}\right)\left(1 + e^{\frac{t-p_6}{p_8}}\right)} \tag{1}$$

The parameter p_1 is the uncorrelated (assumed flat) background, p_2, p_3 and p_4 describe the shape of the central part of the distribution, p_5 is an estimate of t_0 of that given tube, p_6 is the maximum drift time, p_7 and p_8 describe the leading and trailing edges. As an example, a typical drift-time distribution and
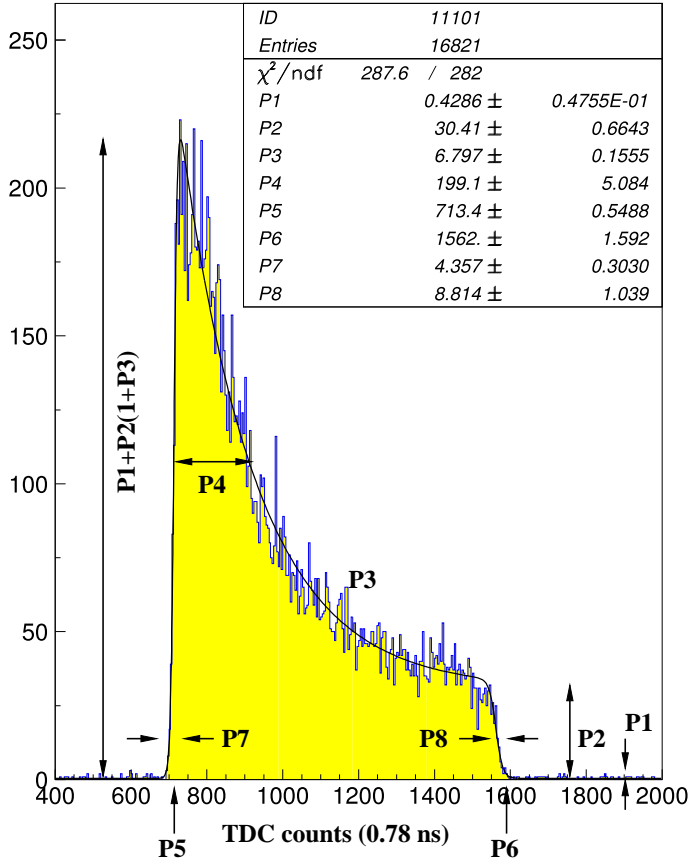
Fig. 2. Typical drift time distribution at nominal operating conditions. The fitted Classic t_0 function described in the text is also shown.

the corresponding fit is shown in Fig. 2. p_5 does not correspond to the start of the physical drift time window but it is close to the half height position of the leading edge and is thus significantly shifted to later times with respect to the start of the physical drift time window. However, as all drift times are related to this value, determined for each tube, the systematic shift will be reabsorbed in the definition of the $r(t)$ relation.

The leading edge slope and p_5 are observed to be correlated. This observation suggests that the start of the MDT drift distribution is better identified by a combination of the two parameters. The use of Monte Carlo generated samples shows that the optimal combination is $t_0 = p_5 - 1.5 \times p_7$. This definition will be used in the rest of the paper. The algorithm gives a resolution of 0.75 TDC counts for samples of 5k events and 0.25 TDC counts for samples of 50k events.

A procedure similar to that used to find the best t_0 indicator has been used to study the measurement of the drift spectrum length t_{max}. The Fermi Dirac function which describes the trailing edge of the drift time spectrum is characterized by a p_6 value and by a trailing edge slope p_8. As in the previous case the drift spectrum length t_{max}, defined to be $t_1 - t_0$, has been studied

10

and found to reach the minimum spread for a value of the correction factor which is equal to 1.2. A resolution of 1.9 and 1.0 TDC counts is observed for sample sizes of 5k and 50k events, respectively.

The drift time distribution depends on a number of environmental parameters like pressure, temperature, B field, gas composition. At H8 there was no B field inside the MDT chambers, the pressure was expected to be stable, the temperature was continuously monitored. The effects of temperature variation are studied in this paper.

Once the drift time has been computed, it is converted into a drift radius assuming an $r(t)$ relation. This relation is determined by an iterative procedure, autocalibration, that minimizes the space residuals in a straight line fit to the drift circles of a candidate track. The procedure starts with a trial $r(t)$ relation to convert the drift time measurements into drift radii that are used in the track fit. The mean value of the residuals, as a function of r, are then used to obtain the first-order correction to the $r(t)$ relation. After a few iterations the minimization procedure converges to a stable solution. As an estimator of the stability of the solutions the mean square correction, defined as $\Delta_k^2 = \sum_j (d_{kj}^2)/N$, is used. In this expression (d_{kj}^2) is the mean value of the residuals in the time bin j for the kth iteration and N is the number of bins. A good solution corresponds to a value of Δ below 20 microns. The mean value of the distribution of the residuals and the number of iterations are figures of merit in evaluating the overall performance of a chamber. All the calibration analysis presented in this work was performed using the Calib program [18].

Comparison between data and the result of the simulation package GARFIELD [19], that describes in details the response of gaz ionization detectors, are discussed in section 4.1.

3.2 Alignment procedures

3.2.1 Alignment devices

The ATLAS muon alignment system [20] is based on optoelectronic sensors that measure the positions and the deformations of the MDT chambers. In addition, temperature sensors are used to correlate chamber expansions with temperature. In the barrel part, the optical sensors are placed on the chambers to directly determine their alignment. In the end-cap, chambers are aligned relative to a set of aluminum bars [21] whose positions and deformations are monitored by optical and temperature sensors.

Two different optical systems are used in the ATLAS alignment: RASNIKs and BCAMs/SaCams. Both systems are based on the principle of a three-point straightness monitor: an optoelectronic image sensor (CCD or CMOS) monitors the position of an illuminated target through a lens. The sensor image is analysed online and converted into four parameters characterising

the deviation from the nominal geometry: two translations perpendicular to the optical axis, the rotation around and the longitudinal position along the axis, the latter being derived from the optical magnification.

In the RASNIK [22] system, an image sensor monitors through a lens an illuminated target carrying a chessboard-like pattern imprinted on a mask. For a symmetric RASNIK with the lens halfway between image sensor and mask, a transverse resolution of 1 μm and a magnification resolution of 2×10^{-5} have been obtained.

The BCAM [24] is a camera consisting of a CCD image sensor which monitors the position of a laser diode through a lens. The BCAM housing also contains a set of two or four laser diodes which can be used as targets by another BCAM. BCAMs are mostly used in pairs, facing each other. The image sensor is placed close to the focal plane of the lens (76 mm), while the target with the laser diodes is placed at a distance of 0.5 m to 16 m. The image of a laser diode on the CCD appears as a circular spot.

BCAMs achieve a relative resolution of 5 μrad for a target distance of 16 m. If the target consists of two or more laser diodes with a known separation, relative angles can be extracted, which yield magnification and rotation around the optical axis. If BCAM's are used in pairs, the absolute angular position of the partner can be determined with 50 μrad accuracy.

Like the BCAM, the SaCam [23] consists of a camera with an image sensor and a lens at fixed distance. The target consists of four back-illuminated holes, covered by a light diffuser. The lens is mounted at distances ranging from 25 mm to 80 mm, depending on the distance between image sensor and target. A relative resolution of 5 μrad has been achieved with the SaCam, a result similar to that of the BCAM.

3.2.2 Barrel alignment setup

The corner stone of the barrel alignment system are optical lines called the *projective* lines, pointing toward the interaction point and connecting the three layers of BIL, BML and BOL chambers. The used technology is the RASNIK system, where the mask is placed on BIL, the lens on BML and the image sensor on BOL chambers. In ATLAS, the 6 MDT towers of one half sector will be typically equipped with 8 projective lines. In H8 the 2 MDT towers were equipped with 8 projective line, leading to an overconstrained system which permits to better study systematic effects.

Besides the projective system, other systems used in ATLAS were studied. These systems are: (1) the inplane system, which monitors deformation of the mechanical structure supporting the multilayer, (2) the axial and praxial system which permits to monitor the translation/orientation of 2 adjacent chambers in one layer, (3) the reference system which permits to monitor the position of the chambers relative to a reference system connected to the coils of the barrel toroid. In H8, the reference system was mounted on a stable

external structure.

3.2.3 End-cap alignment setup

The alignment strategy used in the barrel would require many projective lines of sight traversing the closed vessel of the end-cap toroidal magnets, which turned out to be impossible. The solution that was adopted is a grid of optically connected alignment bars which are used as precision reference rulers. The bars are equipped with internal RASNIKs and temperature sensors to determine their deviations from the initial shape (measured prior to installation with a long range 3D coordinate measuring machine). The spatial relationship between the bars is established by a network of BCAMs on the bars, each measuring the bearing angle of laser diodes on BCAMs on other bars. The chambers in turn are referenced to the alignment grid using the proximity system, where cameras on chambers view RASNIK masks on bars or other chambers, and laser sources on chambers are viewed by BCAMs on bars.

The end-cap setup in H8 corresponds to one octant of an ATLAS end-cap, consisting of six alignment bars and six chambers (two bars and two chambers in each station, EI, EM and EO), and a complete set of alignment sensors.

3.2.4 Alignment software

Two geometry reconstruction software have been developed, called ASAP [14] [25] for the Barrel and ARAMyS [15] [26] for the end-cap. The aim of these 2 packages is to convert the optical sensor measurements into MDT positions, rotations and internal deformations, using standard fitting methods. The main feature of both software packages is their precise description of the optical elements within the barrel or End-cap detector, taking into account all the individual sensor calibration constants which have previously been measured in the laboratories.

Using the same parameters provided by the online image analysis, two alignment modes are implemented, relative and absolute. In the relative mode, the current positions of the MDT chambers are calculated with respect to initial positions - the reference geometry - previously measured by other means, e.g. with straight tracks. In the more ambitious absolute alignment, the positions of the chambers are estimated using only the current measurements. This mode requires an accurate calibration of the geometry of all alignment components.

The resulting data is stored in the Conditions Database for later use by the muon tracking software packages. Both alignment procedures are internal

---

[14] ASAP: **A**tlas **S**pectrometer **A**lignment **P**rogram

[15] **A**lignment**R**econstruction and Simulation for the **A**tlas **My**on **S**pectrometer

to either the barrel or the end-cap part of the Muon Spectrometer; in both the H8 setup and in ATLAS no optical link exists between the Muon Spectrometer and other detectors. Particle tracks will be used for aligning, e.g., the Inner Detector and the Muon Spectrometer.

3.3 Data analysis programs

A prototype of the full ATLAS software chain was tested to analyze the data collected in the H8 test-beam. The event reconstruction was performed within the ATLAS offline reconstruction framework *ATHENA* [27]. The inputs of the muon reconstruction package are the calibration constants, the alignment corrections, and the magnetic field map. In this framework, the various inputs needed to run the reconstruction packages, are stored in a *Conditions Data Base* and are fed to the packages through dedicated *ATHENA services*. During the H8 beam test, the *Conditions Data Base* was operational only for the alignment corrections.

- The *calibration constants* (t_0 and *r(t)* relation) needed to make the transformation from time to radius for each MDT hit were produced for different configurations of H8 test-beam data; they were written to ASCII files and fed to the reconstruction packages through a dedicated *ATHENA service*.
- The *alignment data*, taken asynchronous to the test-beam data every 15 minutes, were written into the *Conditions Data Base* and provided the inputs to the alignment reconstruction packages (ASAP and ARAMyS) which were operated outside *ATHENA*. Using this information, the alignment packages calculated the difference between the nominal detector geometry (provided by the ATLAS muon system data base AMDB) and the actual geometry. The results were written back into the *Conditions Data Base*. A dedicated alignment *ATHENA service* was retrieving the result of the alignment from the *Conditions Data Base* to feed it to the reconstruction packages.
- Finally for the *magnetic field* response a dedicated *ATHENA service* provided the map of the magnetic field at every point in space.

Muonboy is the track pattern recognition program used in the *ATHENA* framework for most of the analysis presented in this paper. The pattern recognition strategy in *Muonboy* is to proceed sequentially through the following steps:

- Identification of regions of activity (ROAs), guided by trigger chamber information
- Reconstruction of local straight track segments in each muon station belonging to a ROA

- Combination of track segments from different muon stations, to form muon candidate tracks
- Global re-fit of muon track candidates using individual hit information.

Details concerning the algorithm can be found in [1]. The command parameters of *Muonboy* can be set to produce straight track segments only, or they can be set to provide fully reconstructed tracks by performing a full fit, which includes the effects of material traversed. Straight track segments were used in this paper for the alignment studies and for the MDT efficiency analysis, whereas fully reconstructed tracks were used to perform tracking analysis.

The analysis of MDT sagitta resolution described in section 6.2 and 6.3 has been performed using the reconstruction algorithm MOORE in the *ATHENA* framework. A detailed description of the MOORE algorithm can be found in [28]. The pattern recognition and track reconstruction steps in MOORE can be summarized as follows:

- Track patterns are built in the x-y plane of the ATLAS reference system, starting from RPC/TGC strips measuring ϕ;
- Track segments in the r-z plane are built from hits in the MDT detectors and combined to ϕ patterns to build roads of hits; the r-z MDT segments are fitted;
- A track is fitted out of each road found in the event, and accepted if the fit is successful.

3.4   Determination of the intrinsic MDT sagitta resolution

The measured sagitta resolution depends not only on the intrinsic chamber resolution and alignment but also on multiple scattering. A momentum scan is thus needed to disentangle the two contributions. The method is described here. The rotating BIL chamber measures the angle (ϑ_{RotBIL}) between the $z-$axis and the muon track upstream of the MBPL magnet (see Fig.1). The barrel chambers measure the same angle for the deflected track downstream of the magnet (ϑ_{barrel}). The track is computed as the line that connects the two super-points associated with the track segments separately in the BIL and BOL chambers, where the super-point is calculated as the crossing point of the track segment, reconstructed through a linear fit of the chamber hits, at the center of the chamber. Using the difference between these two angles ($\Delta\vartheta_B$) the beam momentum is calculated through the formula:

$$p \ (GeV/c) = \frac{0.3BL \ (Tm)}{\Delta\vartheta_B \ (rad)} \tag{2}$$

where BL is the bending power of the magnetic field, which is known as a function of the magnet current. As for a given run, the actual orientation of the

rotating BIL chamber and the barrel chambers is not known, the measurement of the deflections $\Delta\vartheta_B$ as in (2) has to be repeated with the magnetic field switched off ($\Delta\vartheta_0$). The final formula is then:

$$p\ (GeV/c) = \frac{0.3BL\ (Tm)}{(\Delta\vartheta_B - \Delta\vartheta_0)\ (rad)} \qquad (3)$$

The measurement of the momenta cannot be performed in the same way as in ATLAS, since in the H8 setup the tracks crossing the chambers are straight lines. With this method the muon momentum has been measured using the Muon Spectrometer chambers for the first time.

4 Study of MDT calibration constants

A detailed report on the analysis of MDT calibration constants using test beam data can be found in [6]. While t_{max} has a well known and significant temperature and gas composition dependence, t_0 is expected to be almost temperature independent but sensitive to the electronics threshold settings. The effect of the variation of these environmental parameters on t_0 and t_{max} will be studied in sections 4.1 and 4.2 respectively.

4.1 t_0 Systematics

The most illuminated tube of each layer of each chamber was used to study the time stability of t_0. The three barrel chambers and three end-cap chambers give a total of 40 layers. Trace plots of these tubes are observed to be more scattered in summer than in fall runs due to a significant difference in the average run length. The t_0 distribution for each tube and separately for the summer and for the fall, has been constructed and fitted with a Gauss distribution to quantify the stability of the measured t_0 values. The fitted rms width has been taken to be a good indication of the stability of tubes. The width of t_0 fall data taking period is seen to cluster around a value of about 0.5 TDC counts (0.4 ns) dispersion. The spread of t_0 observed during the summer data taking period is larger than in the fall by a factor of about 2 and is again fully understood as being due to a difference in statistics. In particular the t_0 average spread observed in the summer and in the fall agrees well with the calculation described in section 3.1 for an average run length of 5k and 10k events, respectively.
The distribution of the difference of the average t_0 value between summer and fall is shown in Fig. 3. The distribution has been fitted with a Gaussian with an average value of 0.85 TDC counts (0.66 ns) and a rms width of 0.30 TDC
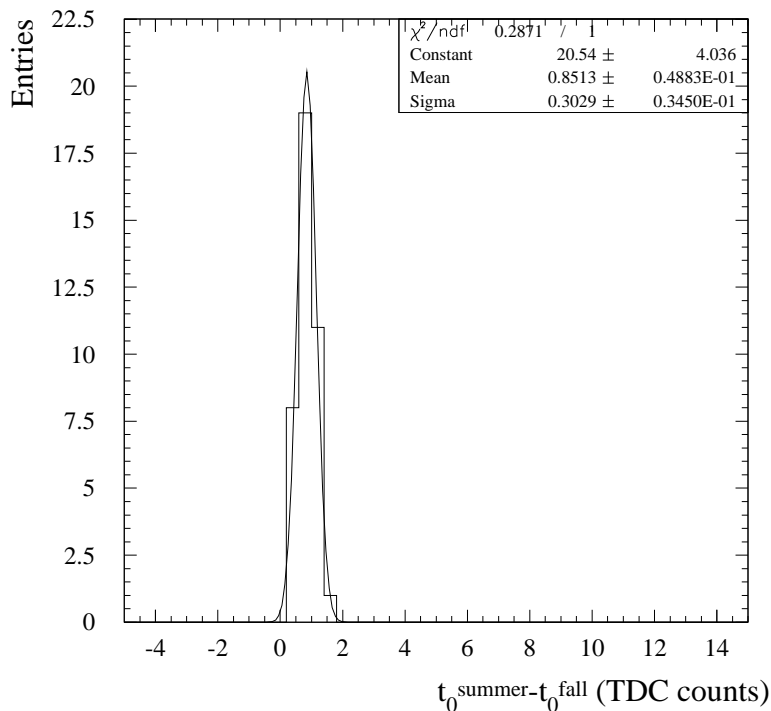
Fig. 3. Distribution of t_0 variation between summer and fall.

counts (0.23 ns). This effect has also been studied using GARFIELD [19]. The predicted shift for a temperature difference of 5^oC was found to be 0.6 ± 0.1 TDC counts ($\sim 0.47 \pm 0.08$ ns), in qualitative agreement with experimental findings. A variation of about $+5°C$ between summer and fall induces an increase of the drift spectrum length (p_6 - p_5) which may result in a change of the correlation between p_5 and p_7. As a counter-proof no significant shift in the t_0 is observed (both in the data and in the simulation) if only the first part of the distribution is fitted using the function of Eq. 1. The observed temperature variation of about $5°C$ between summer and fall induces a reduction of the gas density in a regime of constant pressure which accounts for this effect. At small radii this causes a reduction of the ionization density and thus an increase of the time until the signal crosses the threshold, i.e. t_0. At large radii the reduction of the gas density causes an increase of the drift velocity and a corresponding reduction of the length of the drift time distribution.

The MDT readout electronics has an adjustable discriminator threshold value which affects the value of t_0. Data taken at different thresholds have been used to study the variation of t_0 at different electronics thresholds. Since most data were taken at a threshold value of 40 mV, chosen as the standard working point of MDT chambers, the difference $t_0^{threshold} - t_0^{40mV}$, expected to be the same for all chambers, was chosen to quantify the variation of t_0 with threshold. The same sample of well populated tubes in different cham-
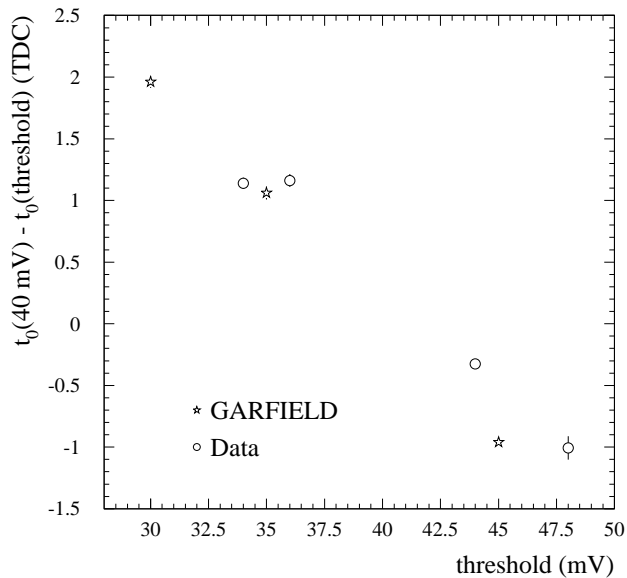
17

Fig. 4. Variation of t_0 as a function of threshold.

bers used in the analysis of stability of single t_0's has also been used to study $t_0^{threshold} - t_0^{40mV}$. Fig. 4 shows $t_0^{40mV} - t_0^{threshold}$ with respect to $t_0^{threshold}$ in the range between 34 and 48 mV for the rotating BIL chamber. Stars were obtained using GARFIELD at 30, 35 and 45 mV. The agreement between data and simulation is good. As expected the slope of the variation is negative and amounts to about 0.13 ns/mV. The same quantity computed using GARFIELD gives a value of 0.15 ns/mV, in good agreement with data.

4.2 t_{max} temperature systematics.

While t_0 is known to have very little temperature dependence, t_{max} is expected to have a significant dependence on temperature. Due to the non negligible systematic temperature difference among the different chambers the comparison of the length of the drift time distribution t_{max} of different chambers was studied as a function of the chamber temperature. The correlation plot between t_{max} and temperature is shown in Fig. 5 for the BIL chamber. The GARFIELD simulation was used to compute t_{max} for a temperature of 27° C and for three different CO_2 fractions of the MDT gas and not considering the presence of other contaminants in the mixture. The point at the nominal gas composition is observed to disagree with data while a good agreement is observed for a gas composition of about $Ar:CO_2$ of 93.5:6.5. It has to be observed that while the gas composition is believed to be stable in time,
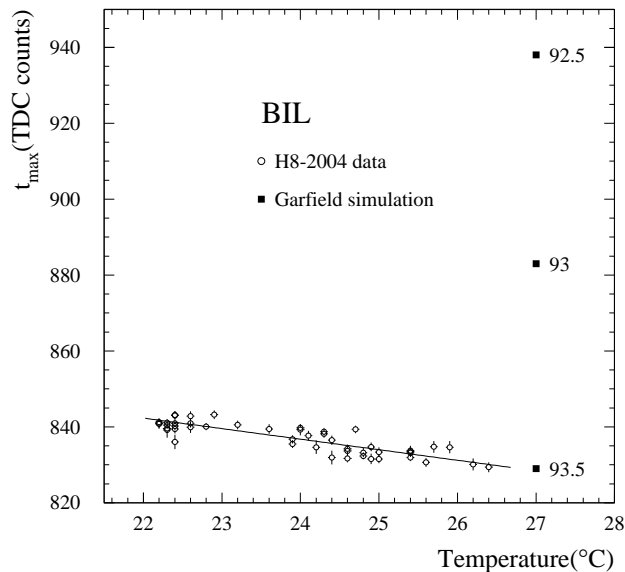
18

Fig. 5. Observed drift spectrum length temperature dependence for the BIL chamber. GARFIELD simulated points at 27° C and for different gas compositions are also shown.

the absolute gas mixture, as produced by the gas system is not accurately known. However, the disagreement can be also explained by the presence of other contaminants as discussed below.

The correlation plot between t_{max} and temperature for different chambers was then fitted with a straight line defined as $t_{max} = \text{(T-24}° C) \cdot \text{slope} + t_{max}^{24°} C$ The average value of the distribution of the slope and of $t_{max}^{24°}$ for the different chambers has a mean value -(2.5±0.1) ns/°C and of 673.9±0.5 ns respectively. The spread of the two distributions is of 0.4±0.1 ns/°C and of 2.0±0.4 ns, respectively. The spread of $t_{max}^{24°}$ is non negligible and can attributed to different gas properties in the different chambers as discussed in section 4.3.

4.3 Study of r(t) relation.

The r(t) relation depends on pressure, temperature and gas composition. The gas distribution system of the H8 setup was made of a single gas mixer which supplies all the chambers. Thus the gas composition (Ar/CO_2 percentage) is assumed to be the same for all chambers while a difference in gas contamination (air or water vapor) and in pressure can occur because of leaks in any gas connection. The only directly measured parameter is the temperature which changes with time and, at the same time, for the different chambers because of the different positions. A mean temperature difference of the order of 5°C is observed between summer and fall while a difference of the order of
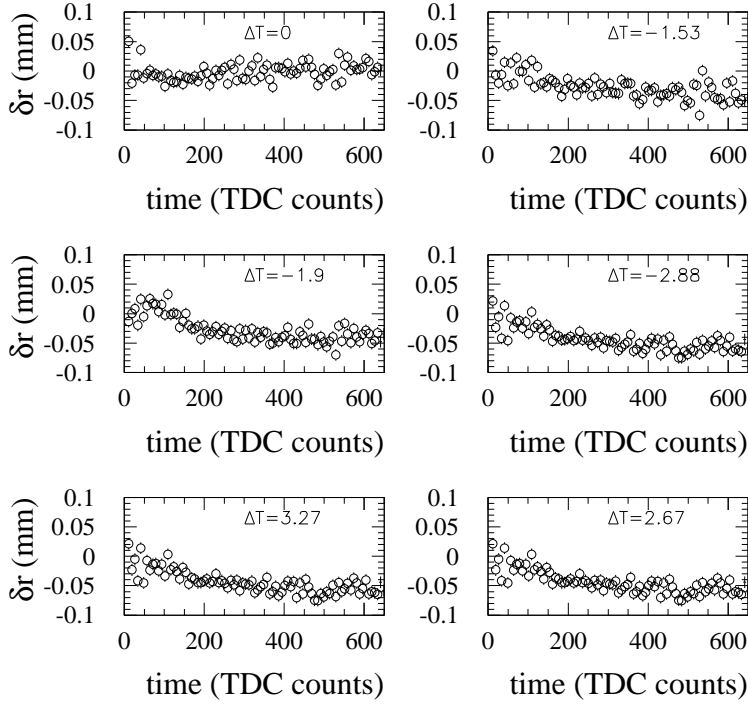
19

Fig. 6. Temperature effects as measured in the summer as obtained using
$BILrot$ data for different temperature variations

$2°C$ is measured between the coldest and the warmest chamber at the same
time.

The effect of temperature variation on the $r(t)$ has already been studied in
laboratory tests [29] and presented as difference between two $r(t)$s as measured
at two different temperatures T_0 and T. The difference has been observed to
vary with the drift time and in particular for a positive temperature difference
it is lower than zero for small drift times (lower than approximately 100 TDC
counts) and smoothly rising for larger drift times up to a value which proved to
scale linearly with the temperature differences as 25 μm/$°C$. In Fig. 6 the $r(t)$
difference as measured in different pairs of runs is shown. These variations,
$\delta r(t)$, can be parametrized with the function:

$$\delta r(t) = \left(\frac{T_0 + \Delta T}{T_0} - 1\right)\left[r(t) - t \cdot \frac{dr(t)}{dt}\right] \tag{4}$$

where T_0 is the reference absolute temperature, $\Delta T = T - T_0$ is the temper-
ature difference, the $r(t)$ function is the one at the reference temperature and
the time derivative of the $r(t)$ function is computed with a fit with Chebytchev
polynomials to the $r(t)$ function at the reference temperature. To check this
parametrization, the parameter ΔT has been determined with a fit to $\delta r(t)$
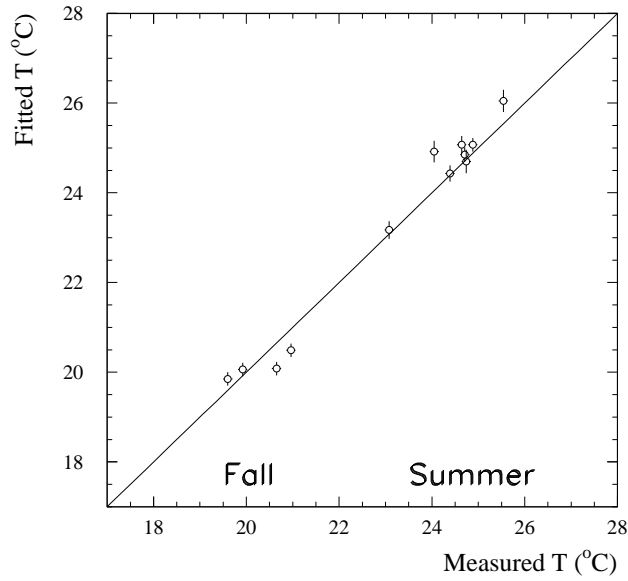
20

Fig. 7. Correlation plot between temperature as measured with probes and as derived from the variation of the $r(t)$ relation in *BILrot* data.
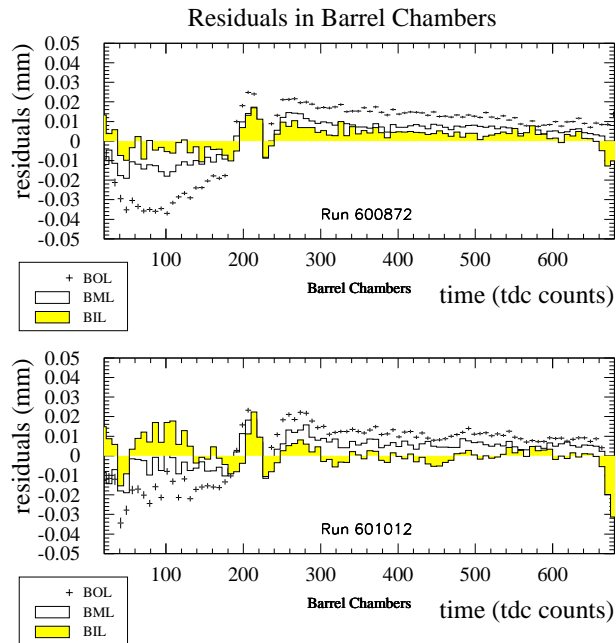

Fig. 8. Residuals versus time for barrel chambers and for two different runs as obtained using a temperature corrected r(t) relation extrapolated from *BILrot*

and compared with the measured temperature changes. This correlation plot as obtained using runs with a 40 mV threshold, with the *BILrot* in rotation by more than 6 degrees and with a number of events larger than 20k, is shown

21

in Fig. 7. It has to be underlined that the set of runs with a temperature lower than 22°C refers to the fall period while the others to the summer time. The line shown in the figure is the bisector line. The good agreement between fitted and measured temperature values over a period of many months indicates the stability of the $r(t)$ over time once corrected for temperature effects using equation (4). The $r(t)$ computed in the rotating BIL can be used for reconstruction in the other chambers as well once corrected for temperature variation. This leads to good average residuals (of less than 20 μm) only if the gas properties of the chamber under study are close to those of the rotating BIL itself.

The temperature correction can be checked, for example, looking at the value of $t_{max}^{24°}$ introduced in the previous section. Fig. 8 shows the average residuals of barrel chambers as a function of time as obtained using a temperature corrected $r(t)$ relation extrapolated from $BILrot$. The two parts of the figure refer to two different runs. Solid line histograms of each part refer to BIL and BML chambers while full points refer to BOL chamber. In both runs the pattern is the same: while the residuals of inner chambers are within 20 μm at all times (and normally less than 10 μm) the BOL chamber shows average residuals that are significantly larger than for the other two chambers. The difference in residuals observed in different chambers can be correlated to the fact that the average t_{max} value of BOL is 4 TDC counts larger than the average of BIL and BML chambers. Furthermore the t_{max} rms value of BIL and BML chambers of 0.70 TDC counts indicates that the difference is statistically significant. The observed change Δt_{max} is expected to induce residuals at a time t of the order $\approx$ $\Delta t_{max}/t_{max}$ $\times$ $v_d(t)$ in good agreement with findings. This finding suggests a slightly different gas composition in the different chambers. In [30] the effect of the presence of water, Nitrogen, Oxygen, Methane in the standard MDT gas mixture has been studied. While water is shown to induce a variation Δt_{max} in the t_{max} value like Δt_{max} $=$ $.066$ ns / (ppm of $water$), the other contaminants have a negligible effect. The observed difference of the t_{max} value between BOL and BIL and BML chambers may then be attributed to the presence of $\approx$ 50 (ppm of $water$) due to the permeability of the plastic gas pipes, the tube O-rings and endplugs to water.

5 Study of MDT chamber alignment

The large amount of data provided by the alignment system of both the barrel and the end-cap muon stand during the 2004 test-beam period has been analysed. Results are presented in this section.
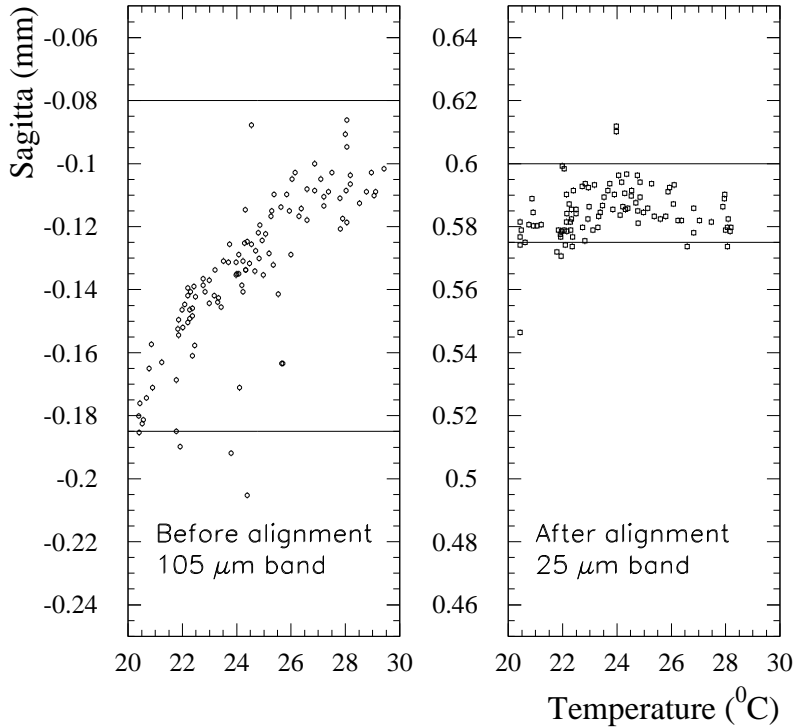
Fig. 9. Left (right) plot: sagitta variations as a function of temperature in the barrel before (after) applying the relative alignment corrections

5.1 Monitoring MDT alignment with optical sensors

The continuous monitoring of chamber distortions and shifts of chambers positions was done with alignment data. The variations of the relative positions of the chambers are mostly due to the daily temperature variations within a chamber itself and are reflected in the change of the mean value of the sagitta distribution. The sagitta was calculated separately in the barrel and the end-cap stands by considering straight track segments. Quality criteria were applied to reconstructed tracks: only one segment per chamber with at most one missing hit. Therefore accepted segments had at least 7 associated hits in the BIL/EIL chambers made of 2 x 4 layers of tubes and 5 hits in the BML, BOL/EML, EOL chambers made of 2 x 3 layers.

5.1.1 Temperature effects

Day/night temperature variations induce large variations of the sagitta of reconstructed muon tracks in the end-cap stand, which covers a period of one week. Before applying alignment corrections, variations of the order of several
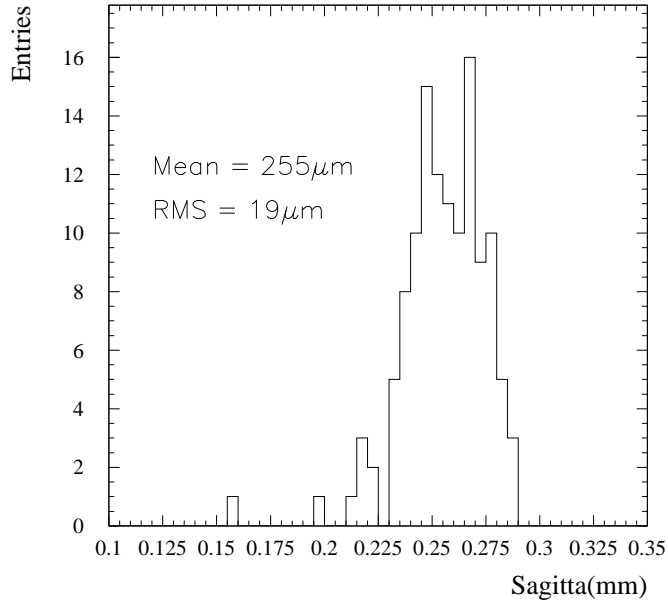
Fig. 10. Mean values of the sagitta in the end-cap, calculated after applying the alignment corrections, for various runs recorded during a one week period. Note that the definition of the sign of the sagitta in this plot is the opposite of what was used in a previous analysis [2].

hundred microns are seen.

In the barrel muon stand the sagitta distribution for events taken over a period of one month is shown in Fig. 9 as a function of the temperature, before (left plot) and after (right plot) applying the alignment corrections. In the barrel stand, the temperature variations explain most of the sagitta variations. Furthermore, the mean values of the sagitta distribution in the barrel muon stand are stable within a few microns over this one month period.

The distribution of mean values of the sagitta distribution in the end-cap, calculated after applying the alignment corrections, is shown in Fig. 10 for a period of one week. The stability of the results is reflected in the rms dispersion of this distribution (19 μm) which is well within specifications.

5.1.2   Controlled movements of barrel MDT chambers

Several runs were recorded to check the response of the alignment system to controlled movements of all barrel MDT chambers in conditions close to the dynamical range of the optical alignment sensors. Translations were in the horizontal Z direction and rotations around the vertical Y axis, parallel to the tubes. Table 1 summarizes the range of these movements. Both alignment modes, relative and absolute, were tested by studying the distributions of the

24

Period	Chamber	Translation	Rotation
not combined	BIL	0 to 20 mm	-8 to +8 mrad
combined	BIL	0 to 4.5 mm	-3 to +2 mrad
	BML	0 to 4 mm	-3 to +3 mrad
	BOL	0 to 6 mm	-2 to 0 mrad

Table 1

Range of barrel MDT movements during the 2004 test beam period.

track sagitta. In July 2004, three runs with barrel chamber movements were taken and data were recorded with a hodoscope triggered beam of pions. The sagitta residuals have a dispersion of 78 μm after absolute alignment corrections and 14 μm in the relative alignment mode. In the November 2004 test beam period, 18 runs were recorded with controlled movements (translations and rotations) of all barrel MDT chambers. This time, a muon beam was used and the trigger was (10 x 10) cm^2. Data from some of these runs were discarded as several optical sensors were either out of range or did not work properly. Results are shown in Fig. 11: before the alignment corrections are applied, the mean value of the sagitta varies by several millimeters reflecting MDT chamber movements. After alignment corrections are applied, all sagitta distributions are centered at the same mean value around zero, as expected. The sagitta residuals have a dispersion of 18 μm in the relative alignment mode. In the absolute mode, the mean value of the sagitta is $\sim 350 \ \mu m$ which indicates that final calibrations of the optical sensors are needed to improve the alignment performance.

This study shows that the geometrical range of operation of the alignment sensors is adequate for accommodating several mm of misplacements of the muon chambers, which is the accuracy achieved when installing some "difficult" chambers in ATLAS. Using the alignment corrections delivered by the system, muons can be reconstructed with the required accuracy.

5.2   Results on alignment with tracks

An essential part of the alignment is to find the initial geometry. This serves as a reference which is extrapolated to any later time using the optical system in relative mode. A survey may be used for this, but it lacks the necessary precision and it cannot be performed for the entire ATLAS spectrometer. Therefore the initial geometry needs to be determined with tracks. The H8 test beam data were used to check the feasibility of this method.
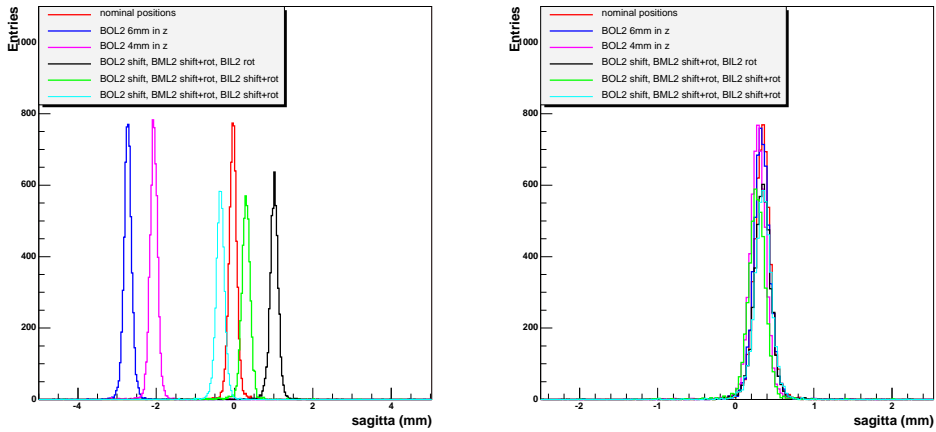
Fig. 11. Left plot: sagitta distribution for 6 runs in which different controlled movements of MDT chambers were performed, before alignment corrections. Right plot: sagitta distribution for the same runs, after applying the absolute alignment corrections.

Tools to perform alignment with straight tracks have been developed [7] and applied in several H8 runs. A track may be seen as a collection of hits, produced by a pattern recognition algorithm. A χ^2 function is built for each track, which will depend on track parameters and on the spatial coordinates and orientation of the sensitive devices producing the hits. The alignment consists in finding the best set of track and chamber parameters using a sample of several thousand tracks. An optimizing track fitting procedure is developed for that purpose.

For performing track-based alignment, it is essential to illuminate the largest possible portion of the chambers with the beam. Given this requirement, only runs recorded using the hodoscope trigger were used. However, tracks from hodoscope samples are parallel at the level of 5 $mrad$, and also, the illuminated portion of the chambers, even with the hodoscope runs, is very small. This implies that some degrees of freedom may not be fitted at H8. The alignment obtained using tracks was found to be consistent with the survey positions and with the movements of the chambers that were made between the period of the survey and the period of the recording of the run. Fig. 12 shows the sagitta of the selected tracks, before and after the alignment fit. The mean value of the sagitta is corrected within 5 μm, and the width of the distribution is also improved.

In order to assess the performance of the track-based alignment, a procedure was set up to compare it with the optical relative alignment. The starting point is a pair of runs, between which some movements of the chambers have been performed. Track-based alignment is applied to these two runs producing the alignment corrections A_1 and A_2. The first set of corrections A_1 is then used as reference geometry for $ASAP$ in relative mode, which can in turn extrapolate the geometry to the period of the second run by using the response
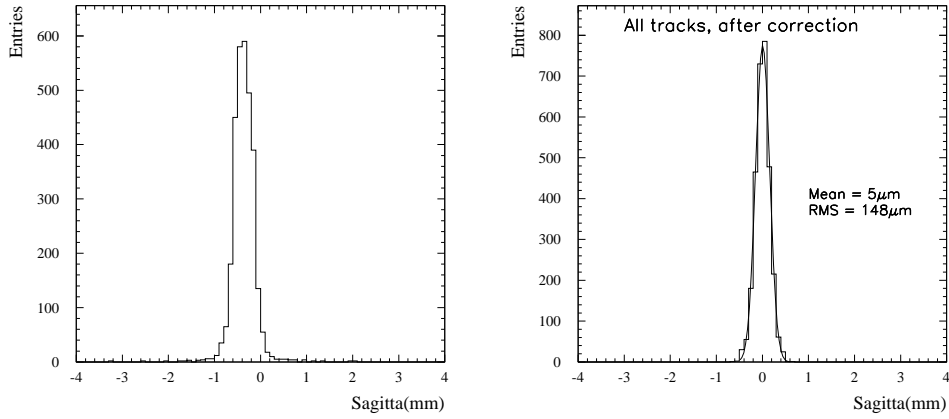
Fig. 12. Sagitta distribution of selected tracks before and after the alignment fit. Left: Distribution of sagitta of selected tracks with the chambers at the survey position. The muon sagitta is centered at -351 microns. Right: Distribution of sagitta after alignment fit. The mean value of sagitta is now 5 microns.

of the optical sensors only. This extrapolated alignment will be called A_2'. If there is no systematic bias, then A_2 and A_2' should both result in a similar sagitta distribution. Fig. 13 shows the sagitta of reconstructed tracks for alignments A_2 and A_2' performed on data from the second run, after rotating the BIL chambers by 6 $mrad$ around the beam axis. The two alignments show similar small biases on the sagitta (34 and 39 μm). The track-based alignment
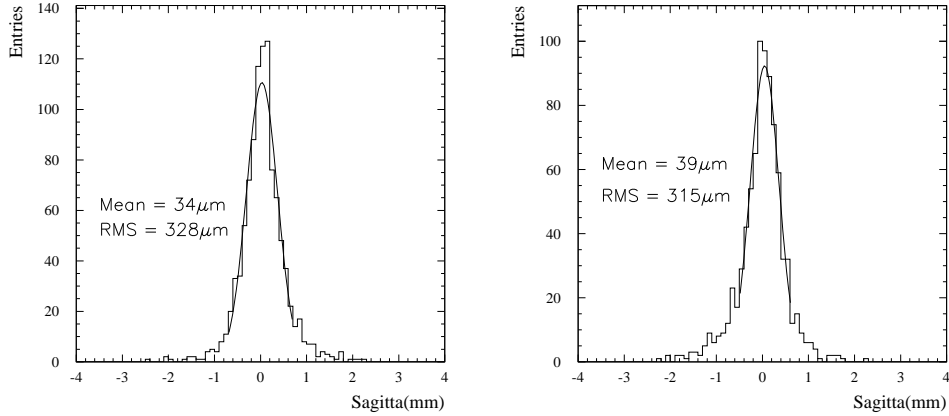
Fig. 13. Sagitta distribution of tracks in a run where the BIL chambers were rotated by 6mrad around the beam direction. Left: after track-based alignment corrections (alignment A2 in the text). Right: track-based alignment is performed on a run where the chambers were in the nominal position and "ASAP" alignment corrections in relative mode is used to extrapolate the alignment to the time of the plot (alignment A_2' in the text).

appears to be very precise in the degrees of freedom to which H8 tracks are sensitive. The feasibility study shows that the initial geometry can certainly be determined in ATLAS, given a sample of straight tracks. In ATLAS additional degrees of freedom wil be fitted, given that the tracks will have a larger angular spread. A combination of cosmics tracks and tracks issued from collisions where the toroid magnet is off is foreseen for that purpose.

5.3 Combining tracks in the Inner Detector and the Muon Spectrometer

With the combined test beam data it is possible to correlate measurements made in the muon spectrometer with those made in other detectors of the setup. The track reconstruction in the Inner Detector is performed by the *StraightLineFitter* package and the track reconstruction in the muon system is performed using *Muonboy*. The track correlation is evaluated at the perigee ($x = 0$). The muon track needs to be extrapolated back to the perigee, taking into account the substantial energy losses in the calorimeters and the iron dump. This back-tracking is performed within *Muonboy* which uses a detailed description of the H8 setup (geometry and material). The correlation in the z coordinate (the precision coordinate for MDT's), shown in Fig. 14, has a slope compatible with 1. The $-7.9\ mm$ offset represents the small misalignment of
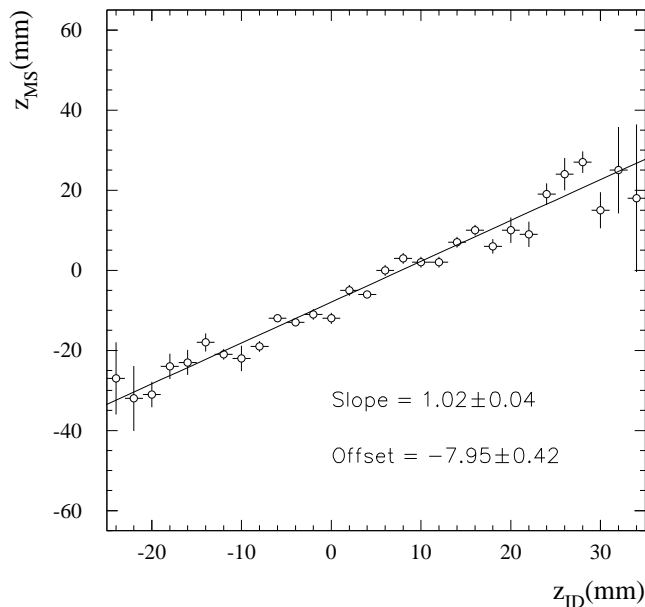

Fig. 14. Correlation between the muon system tracking and the Inner Detector tracking.

28

the Inner Detector with respect to the muon system.

The accuracy of the relative alignment of the Muon Spectrometer and the Inner Detector is limited by and depends crucially on the multiple scattering of particles in the material between these two detectors. A detailed description of this material will be needed by the reconstruction programs in ATLAS.

6 Reconstruction efficiencies and sagitta measurement

In this section, the efficiency for reconstructing track segments is studied and the single hit efficiency for MDT chambers is calculated for various operational conditions. The data used in these studies, come from runs recorded with the (10 x 10) cm^2 trigger for a number of H8 beam energies and MDT operational thresholds. The runs analysed were restricted to those where the beam was deflected into the second BML chamber by the BMPL magnet to prevent the beam from crossing the boundary area between the adjacent BML chambers, a source of large inefficiency. The track segment efficiency of one MDT chamber is calculated as follows.

Two of the three stations (barrel or end-cap) belonging to the same tower are chosen as reference stations, the third being the tested station. Only events with one reconstructed segment in each reference station, are accepted, with a total number of hits not smaller than $(n_{total} - 1)$, where $n_{total} = 8$ or 6 is the number of tube layers in a given chamber, as described in 5.1. With the two reconstructed segments of the reference stations, the sagitta is calculated for all the reconstructed segments of the tested station. The sagitta distribution, with standard deviation σ, is used to select good segments in the following way: the segments with the correct minimum number of hits and within $\pm (n \times \sigma)$ of the mean value are counted as good segments. The ratio of good segments to the reference sample reaches a plateau after $3 \times \sigma$. A fit of the plateau region with a constant level is assumed to be representative of the track segment efficiency. This method is applied to both the barrel and end-cap chambers and the results are presented in Table 2.

By analysing runs with various beam energies, it was found that the track segment efficiency is independent on particle momentum for the nominal MDT threshold (40 mV) as expected. The effect of varying the threshold is shown in Fig. 15: the track segment efficiency is stable for thresholds above the nominal value and drops by $\approx 1\%$ for the lower threshold (36 mV) and by $\approx 2\%$ when the most stringent requirements are used. This efficiency drop is due to the increased noise when the MDT signal threshold is lowered.

Track segment efficiency (%)			
Barrel chamber (n_{total})	BIL (8)	BML (6)	BOL (6)
$N_{hits} \geq n_{total}\text{-}1$	93.2 ± 0.2	94.3 ± 0.1	96.3 ± 0.2
$= n_{total}$	68.2 ± 0.3	71.5 ± 0.3	76.3 ± 0.4
End-cap chamber (n_{total})	EIL (8)	EML (6)	EOL (6)
$N_{hits} \geq n_{total} - 1$	89.8 ± 0.2	94.9 ± 0.2	95.3 ± 0.1
$= n_{total}$	63.7 ± 0.3	74.4 ± 0.4	75.6 ± 0.2

Table 2

Track segment efficiency (%), for different number of hits, for barrel and end-cap chambers. The number of tube layers n_{total} is indicated for each type of MDT chamber. The threshold is nominal, at $40 \ mV$.
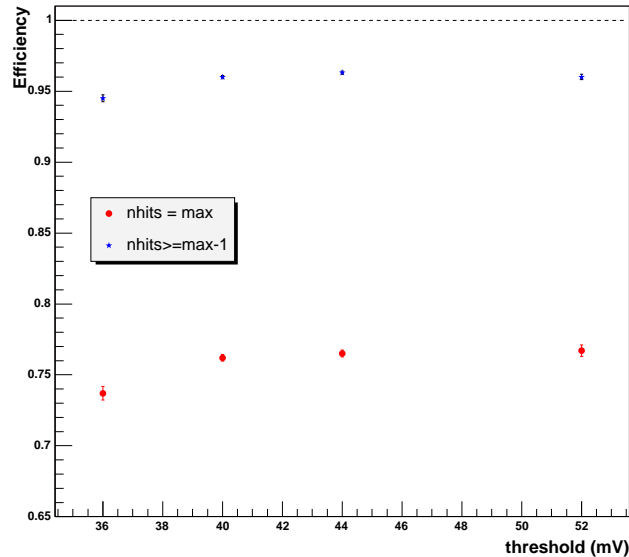
Fig. 15. Track segment efficiency versus MDT threshold of the EOL chamber, for two cases: a) when the most stringent requirement to validate a track segment ($N_{hits} = n_{total}$) and b) when ($N_{hits} = n_{total} - 1$) are used. The beam momentum is 180 GeV/c.

6.1 Hit and track efficiency

The track segment efficiency ($\epsilon_{segment}$) is related to the single hit efficiency (ϵ_{hit}) through:

$$\epsilon(n_{hits}/n_{total}) = \epsilon_{segment} = \frac{n_{total}!}{n_{hits}!(n_{total} - n_{hits})!}(\epsilon_{hit})^{n_{hits}}(1 - \epsilon_{hit})^{n_{total}-n_{hits}}$$

$$(5)$$

where n_{hits} is the minimum number of required hits and n_{total} is the total number of possible hits in a segment. Table 3 shows single hit efficiencies, extracted from the track segment efficiencies, for barrel and end-cap chambers and for two cases: $n_{hits} = n_{total} - 1$ and $n_{hits} = n_{total}$. Similar single hit efficiencies are found for both the barrel and end-cap chambers, as expected.

The measured single hit efficiencies of $95 - 96\%$ are in line with previous measurements [18] and with expectations from simulations documented in [1] (p. 178), where a 5% inefficiency is attributed to the walls of the tubes and to δ-ray electrons which obscure the muon signal.

Single hit efficiency (%)			
Number of required hits	BIL	BML	BOL
$= n_{total}$-1	95.8 ± 0.1	95.1 ± 0.2	95.9 ± 0.2
$= n_{total}$	95.3 ± 0.1	94.6 ± 0.1	95.6 ± 0.1
N_{hits}	EIL	EML	EOL
$= n_{total}$-1	95.5 ± 0.1	95.8 ± 0.2	95.9 ± 0.2
$= n_{total}$	94.5 ± 0.1	95.2 ± 0.1	95.4 ± 0.1

Table 3

Single hit efficiency (%), for different number of hits, for barrel and end-cap chambers

For some runs of the last running period (November 2004), a $(15 \times 15 \times 1)$ cm^3 block of stainless steel was placed in the beam path in front of all barrel chambers, BIL, BML and BOL. This was done to study the effect of this added material on the performance of the pattern recognition algorithm. The analyzed runs were at a fixed beam energy. A 1% drop of the single hit efficiency in the presence of material is observed.

6.2 Sagitta measurement

The momentum measurement has been performed as described in section 3.4. For each beam momentum, first the angular difference $\Delta\vartheta_0$ has been measured to correct for misalignment due to rotation about the $y-$axis. Then, $\Delta\vartheta_B$ has been computed. The distributions of the two angular differences are shown in Fig. 16 for the runs with 120 GeV/c nominal beam momentum and 40 mV threshold. Also the measured momentum spectrum, computed with equation (3), is shown. The measured momentum distributions for all the data sets at the 44 mV threshold, are illustrated in Fig. 17. In Table 4, the mean values and the standard deviation of the momentum distributions at

the three different threshold, obtained with a Gaussian fit are shown. The difference observed between the nominal and measured momentum is mainly
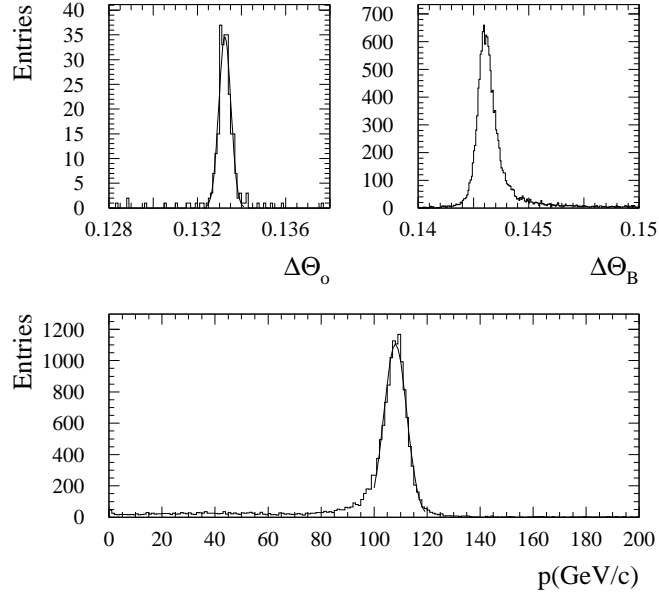

Fig. 16. Top left: the distribution of $\Delta\vartheta_0$. Top right: distribution of $\Delta\vartheta_B$. Bottom: distribution of the beam momentum. The figures refer to the data set at 120 GeV/c.
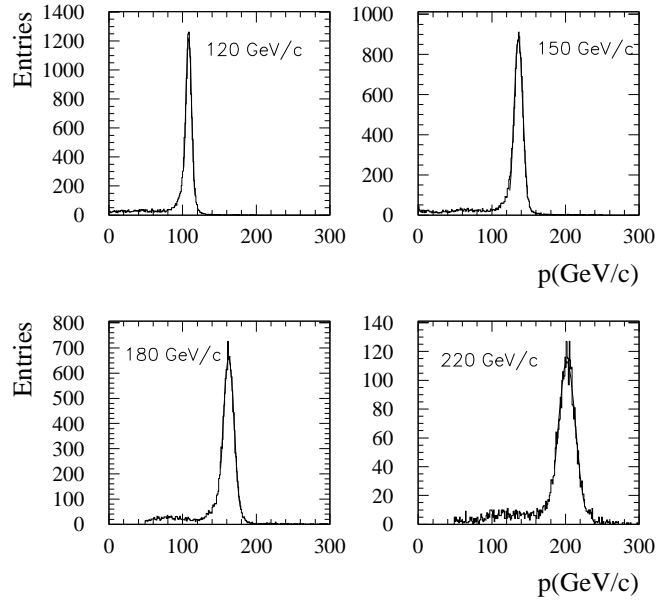

Fig. 17. Momentum distribution for the different samples at 44 mV threshold.

32

due to the beam energy loss in the calorimeter material and in the beam dump, upstream of the muon area.

The sagitta resolution for each data set has been evaluated after two cuts. First RPC strips have been used to select events crossing a limited portion in the Y coordinate of the MDT tubes. Second only events with a momentum larger than $p_{mean} - 2\sigma_p$ have been selected. The final sagitta distributions are shown in Fig. 18 for the 44 mV threshold. The mean sagitta value and standard deviations obtained with the Gaussian fit are reported in Table 5.

The measured sagitta resolution as a function of the measured momentum

Nominal momentum (GeV/c)	36 mV		40 mV		44 mV	
	p_{mean} (GeV/c)	σ_p (GeV/c)	p_{mean} (GeV/c)	σ_p (GeV/c)	p_{mean} (GeV/c)	σ_p (GeV/c)
100	88.7	4.5	88.8	4.2		
120			108.0	4.2	108.1	4.1
150	136.9	6.1	135.0	5.8	136.1	6.0
180	163.5	7.5			163.4	7.4
220	203.2	11.6	206.7	11.3	202.9	11.5
250	229.4	14.9	230.1	15.1		

Table 4

Measured momentum mean value (p_{mean}) and the standard deviation (σ_p) at different nominal momenta for the three thresholds.

Nominal momentum (GeV/c)	36 mV σ_S (μm)	40 mV σ_S (μm)	44 mV σ_S (μm)
100	98 ± 2	102 ± 1	
120		90.6 ± 0.8	92 ± 1
150	75 ± 1	76.5 ± 0.6	78.8 ± 0.8
180	70 ± 1		71.5 ± 0.7
220	63 ± 2	65 ± 2	67 ± 1
250	60 ± 2	62 ± 1	

Table 5

Measured sagitta resolution for different beam momenta after applying the constraints described in the text.
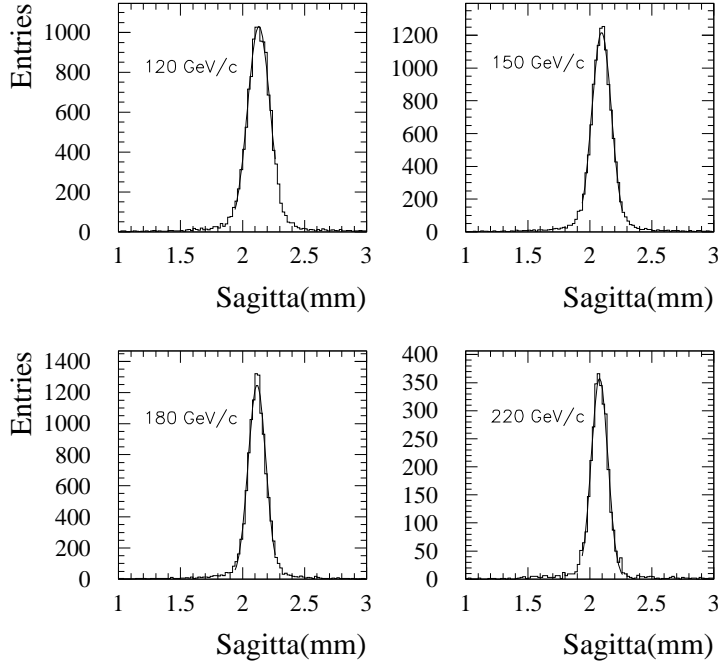
Fig. 18. Measured sagitta at different momentum beam after applying constraints described in the text for the 44 mV threshold.

for three different thresholds is shown in Fig. 19 using the standard deviation of the sagitta distributions reported in Table 5, and the mean value of the beam momentum reported in Table 4.

6.3 Multiple scattering effect on sagitta resolution.

The measured sagitta resolution depends mainly on two independent terms: the intrinsic resolution determined by chamber resolution and alignment, that is a constant term independent of beam momentum, and the multiple scattering, that depends on muon momentum. The points of Fig. 19 have been fitted with equation (6):

$$\sigma = \sqrt{P_1^2 + (P_2/p)^2} \qquad (6)$$

where p is the momentum, P_1 is the constant term related to intrinsic resolution and P_2 is the term related to multiple scattering. The term of intrinsic resolution obtained from the fit at the different thresholds are reported in Table 6. No dependence on electronics threshold is observed.

The P_2 term can be translated into the term $< x/X_0 >$ that is the average thickness crossed by the track in radiation length units. The method reported in Fig. 20 has been used to perform the calculation. It has been assumed the
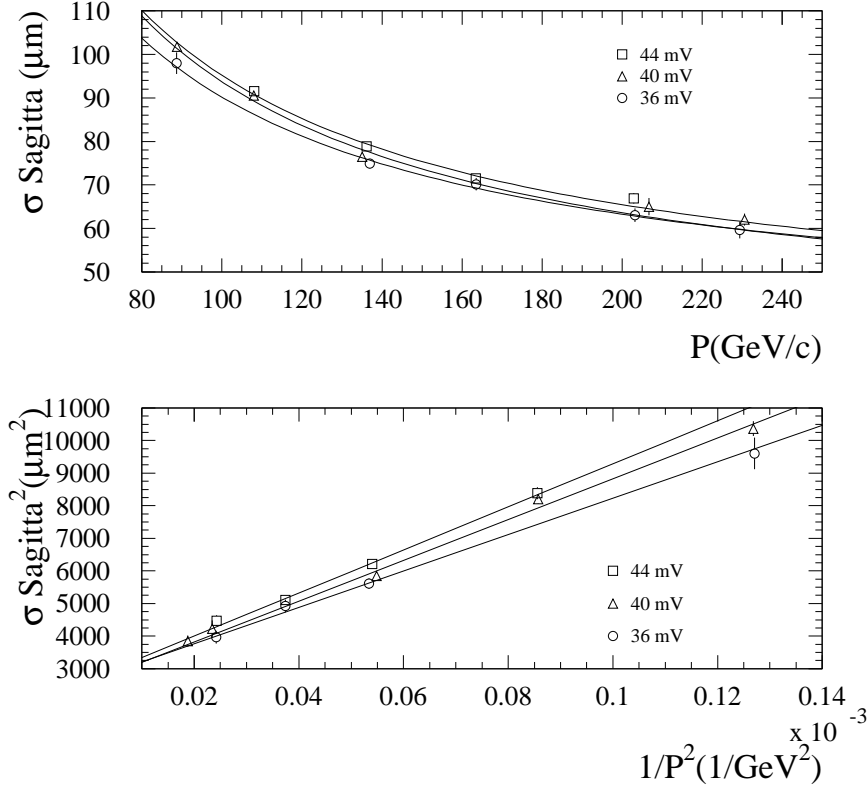
34

Fig. 19. Sagitta resolution as a function of momentum (top) and as a function of 1/p (bottom). The extrapolation and its error when the momentum tends to infinity are immediate in the bottom plot.

Threshold (mV)	Intrinsic sagitta resolution (μm)
36	51.8 ± 1.9
40	50.7 ± 1.5
44	52.3 ± 1.7

Table 6

Intrinsic sagitta resolution values obtained by fit at the different thresholds

scattering takes place exactly at the BML super-point. The sagitta resolution term related to multiple scattering is given by the formula :

$$\sigma_s(multiple\ scatt) = \frac{P_2}{p} \simeq \frac{(z_2 - z_1)(z_3 - z_2)}{(z_3 - z_1)}\sigma_{\theta_0} \qquad (7)$$

where $(z_2 - z_1), (z_3 - z_2)$ and $(z_3 - z_1)$ are the known distances between the chambers, σ_{θ_0} is the r.m.s. of the multiple scattering angle $\simeq \frac{13.6 MeV}{p}\sqrt{x/X_0}$. The relationship between P_2 and $< x/X_0 >$ is then given by the following
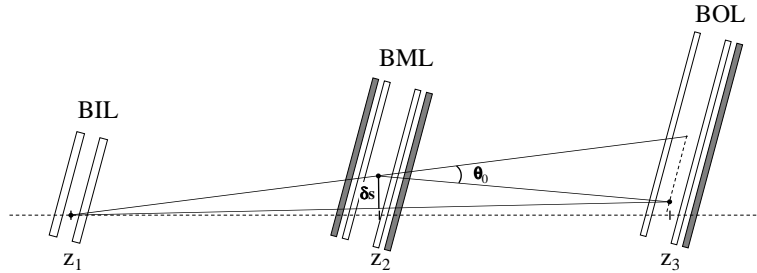
Fig. 20. A top schematic view of the barrel chambers. The method to evaluate the multiple scattering contribution to sagitta resolution is shown.

expression:

$$P_2 \simeq \frac{(z_2 - z_1)(z_3 - z_2)}{(z_3 - z_1)} 13.6 MeV \sqrt{< x/X_0 >} \tag{8}$$

The values of $< x/X_0 >$ obtained by the fit are reported in Table 7. This term accounts for about 8 mm of aluminum of MDT tubes and for the material of the two RPC chambers. As expected the values of $< x/X_0 >$ are compatible with each other within statistical errors.

Threshold	$< x/X_0 >$
36	26.1 ± 2.1
40	29.3 ± 1.0
44	30.5 ± 1.7

Table 7
$< x/X_0 >$ values (in %) obtained by the fit at the different thresholds. All $< x/X_0 >$ values are statistically compatible and give an average of 29.1%±0.8%.

6.4 Muon catastrophic energy losses in Calorimeters

Muons traversing matter lose energy mainly via ionization. Their energy loss increases with increasing momentum. After a critical energy, radiative mechanisms become the major contribution to the energy loss and produce large tails in the energy loss spectrum. The probability for muons to suffer a severe energy loss, known as catastrophic, increases after the critical energy. Energy loss parametrization can only account for the ionization mechanism and should be complemented with direct measurement of the energy loss in the calorimeters before the Muon Spectrometer.

The total energy deposited in the calorimeters for these data was estimated by measuring the energy response in LAr calorimeter and in each of the Tile compartments. In the Tile, given the narrow beam profile and the large granularity of the compartments ($\Delta\eta \times \Delta\phi = 0.1 \times 0.1$ and 0.2×0.1 in the last
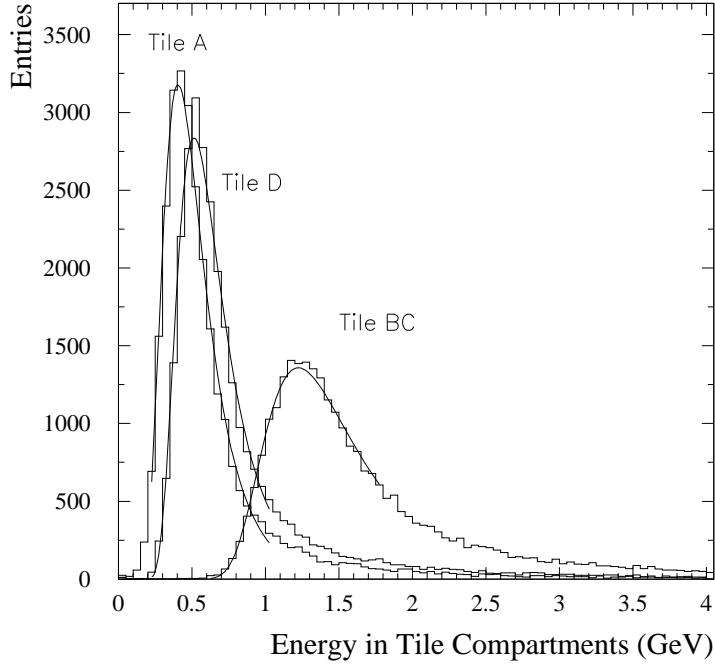
Fig. 21. Energy deposition in the Tile calorimeter.

layer) only the most energetic cell in each layer was added to the total energy. In LAr the most energetic cell from each compartment and its neighbours in η and ϕ with energy 2σ above the noise were added to the total energy.

On the basis of the energy deposited in LAr and in each one of the three Tile compartments events were classified in two mutually exclusive categories:

- Muons with no catastrophic energy loss were required to have a track in the Muon Spectrometer and energy loss of a Minimum Ionizing Particle (MIP) in LAr and in each one of the Tile compartments. The MIP upper energy value was taken as the value 5σ's away from the most probable value of the muon energy loss distribution, obtained from fitting a Landau distribution to the data. The muon energy loss distribution in each of the Tile compartments is shown in Fig. 21. The corresponding MIP upper energy was 0.8 GeV, 2.2 GeV and 1 GeV in each of the three compartments respectively. In LAr the MIP upper energy range is 1.5 GeV.
- Muons with catastrophic energy loss were required to have a track in the Muon Spectrometer and energy deposition larger than the MIP upper energy in one or two consecutive calorimeter compartments, where LAr is treated as a compartment.
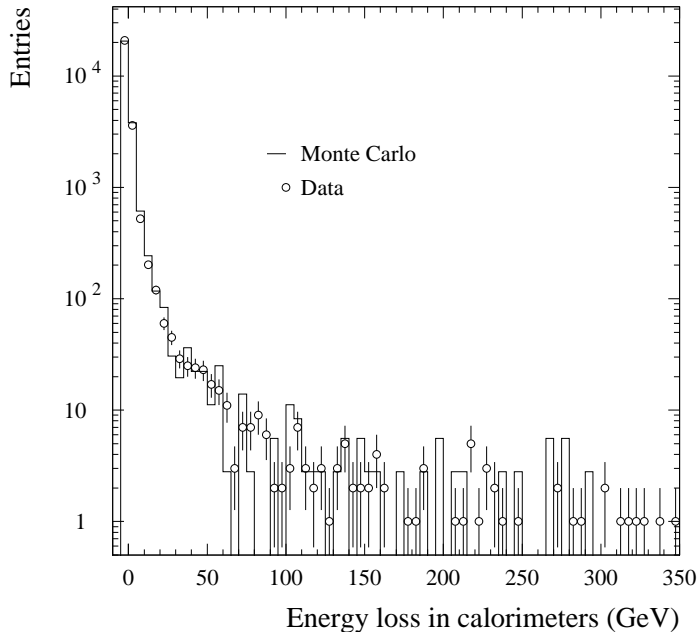
37

Fig. 22. Energy deposited in the calorimeters by particles tagged as muons.

The total energy deposited as measured in the calorimeters, for all muon events in a sample at 350 GeV momentum is shown in Fig. 22. The shape of the spectrum is consistent with the energy loss expected for muons. The agreement with MC expectations is good. The probability for a muon to suffer energy loss above a threshold is computed on the basis of the above results and shown in Fig. 23. In the same figure the values obtained from Monte Carlo are superimposed.

7   Summary

Results obtained using large samples of test beam data taken in the H8 beam line at the CERN SPS in 2004 are presented in this paper. The ATLAS offline framework *ATHENA* was used for reconstruction.

The analysis has shown that the MDT drift time constants are stable over time. This result is reproduced for all chambers and the time stability was observed over a period of several months. The variation of the maximum drift time t_{max} with temperature has also been studied and a linear dependence of t_{max} with respect to temperature with a slope of 2.5 ns/°C was found in agreement with previous measurements.

The *r(t)* relation has also been studied using data from an MDT chamber mounted on a rotating support which allowed a proper angular spread for the
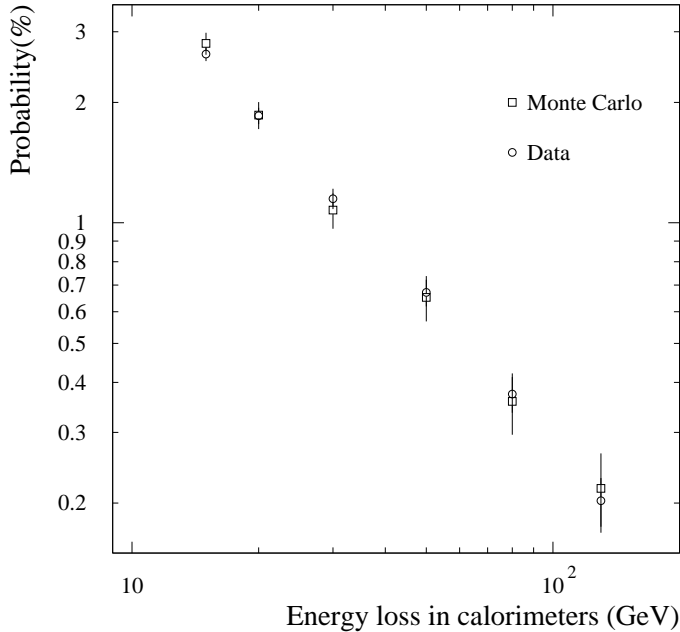
Fig. 23. Probability(%) for catastrophic E_{loss} vs E_{loss}^{tot} in the calorimeters.

calculation. Once corrected for trivial temperature effects, the $r(t)$ relation is found to be stable in time.

Results on the alignment of MDT chambers using optical sensors were presented. Both alignment modes (relative and absolute) were studied. The results are within specifications for both the barrel and end-cap relative alignment, where a precision of approximately 20 μm was obtained. For the absolute mode, the mean value of the sagitta calculatted by optical means is off by 350 μm in the barrel and 250 μm in the end-cap, compared to the one calculated with straight tracks. This shows that some of the calibration entered for the optical alignment sensors, have still to be understood. The concept of alignment was tested and validated for the first time using straight tracks from the H8 data. Finally, a first attempt of relative alignment between the Inner Detector and the Muon Spectrometer was also performed. An offset of -7.9±0.4 mm of the muon system with respect to the Inner Detector was measured over a distance of about 40 meters.

MDT chamber efficiencies were tested for different beam energies, MDT thresholds, and in the presence of material in front of the chambers. Single hit efficiencies, derived from measured track segment efficiencies, are above 95 % for all chambers as expected from simulations.

An intrinsic sagitta resolution of 51±1 μm was measured, in good agreement with the MDT design performance. The sagitta resolution as a function of the muon momentum has been measured for momenta ranging from 100 GeV/c to 250 GeV/c, and for various electronics threshold settings on the

39

MDT precision tracking detectors. Within the statistical errors no dependence of the sagitta resolution on electronics threshold settings has been observed. The beam momentum was measured at the entrance of the barrel Muon Spectrometer sector, to account for energy losses in the upstream material, and remove tails in the beam energy distributions. The sagitta dependence on beam momentum makes it possible to disentangle the contributions coming from multiple scattering and the intrinsic resolution of the tracking detectors.

The study of muon catastrophic energy losses was also made possible by the use of calorimeter data. Results are compared with Monte Carlo simulation and found to be in very good agreement.

With the results presented in this paper, the basic parameters determining the performance of the ATLAS Muon Spectrometer have been measured and found to be within design specifications. They include MDT drift space-time calibrations, optical alignment of muon chambers, alignment with straight tracks, single hit efficiency of MDTs and sagitta resolution as a function of particle momentum. The H8 beam test experiment also constituted an excellent training ground for the actual commissioning of the ATLAS detector.

NOTE: Referenced ATLAS notes are public on the web site
http://cdsweb.cern.ch/collection/ATLAS.

References

[1] The ATLAS Muon Spectrometer Technical Design Report, CERN-LHCC/97-22 (1997);
S. Palestini, Nuclear Physics B (Proc.Suppl.) 125 (2003) 337.

[2] C. Adorisio et al., System Test of the ATLAS Muon Spectrometer in the H8 Beam at the CERN SPS, ATL-MUON-PUB-2007-005, submitted to Elsevier.

[3] Inner Detector Technical Design Report, CERN-LHCC/97-16 and CERN-LHCC/97-16 (1997).

[4] Tile Calorimeter Technical Design Report, CERN-LHCC/96-42 (1996).

[5] Liquid Argon Calorimeter, Technical Design Report, CERN-LHCC/96-41 (1996).

[6] A. Baroncelli et al., Study of MDT calibration constants using H8 testbeam data of year 2004, ATL-MUON-PUB-2007-004.

[7] P.F. Giraud et al., Track-based absolute alignment in the ATLAS muon spectrometer and in the H8 test beam, ATL-MUON-PUB-2006-012.

[8] F. Bauer et al., ATLAS 2004 Combined Test Beam results: Muon Chamber Alignment and Muon Reconstruction, ATL-MUON-PUB-2007-003.

[9] G. Avolio et al., ATLAS Muon Barrel Sagitta Resolution versus Momentum at 2004 H8 Test Beam and comparison with Geant4 Simulation, ATL-MUON-PUB-2006-011.

[10] T. Bachas et al., Studies of catastrophic muon energy losses in ATLAS H8 combined Testbeam data - in publication on Nuclear Physics B, Proceedings Supplement.

[11] M. Livan, Monitored drift tubes in ATLAS, Nucl. Instr. and Meth. in Phys. Res. A384 (1996) 214;
F. Bauer et al., Construction and test of MDT chambers for the ATLAS muon spectrometer, Nucl. Instr. and Meth. in Phys. Res. A461 (2001) 17.

[12] A. Di Ciaccio, Resistive Plate Chambers in ATLAS, Nucl. Instr. and Meth. in Phys. Res. A384 (1996) 222;
A. Aloisio et al., The Trigger Chambers of the ATLAS Barrel Spectrometer: Production and Tests, Nucl. Instr. and Meth. in Phys. Res. A535 (2004) 265.

[13] J. Chapman et al., Data flow simulations through the ATLAS Muon front-end electronics, Proceedings of the 5th Conference on Electronics for LHC Experiments, Snowmass, CO, USA, 20-24 September 1999, p.448.

[14] H. Beterenbrood et al., The Read Out Driver for the ATLAS MDT Muon Precision Chambers, IEEE Trans. Nucl. Sci. 53 (2006) 741.

[15] S. Tanaka et al., Techniques Developed for the ATLAS Thin Gap Chambers Mass Production, IEEE Trans. Nucl. Sci. 51 (2004) 934.

[16] M. Boterenbrood et al., Design and implementation of the ATLAS detector control system, IEEE Trans. Nucl. Sci., 51 (2004) 495-501;
M. Boterenbrood, B. Hallgren, The development of Embedded Local Monitor (ELMB), Proceedings of the 9th Workshop on electronics for the LHC Experiments, LECC 2003, Amsterdam, The Netherlands, 29 Sep - 3 Oct 2003, p.331-334;
J. Rothberg, Detector Control Systems in the LHC Experiments, 9th Workshop on Electronics for LHC Experiments, Amsterdam, Netherlands, 29 September 2003.

[17] M. Aleska, W. Riegler, Non linear MDT drift gases like Ar/CO2, ATLAS Internal Note, ATL-MUON-98-268.

[18] P. Bagnaia et al., CALIB: a Package for MDT Calibration Studies, ATL-MUON-2005-013 (2002);
G. Avolio et al., Test of the first BIL tracking chamber for the ATLAS muon spectrometer, NIM A523(2006) 309.

[19] R. Veenhof, GARFIELD, Recent Developments, Nucl. Instr. and Meth. in Phys. Res. A419 (1998) 726.

[20] C. Amelung et al., The alignment system of the ATLAS muon spectrometer, Eur. Phys. J. C33, s01 (2004) 999.
Ch. Amelung et al, Results on the Test of the Muon End-Cap Alignment system in the H8 Beam Line, ATL-MUON-2004-009.

[21] C. Amelung et al., Reference Bars for the Alignment of the ATLAS Muon Spectrometer, Nucl. Instr. and Meth. in Phys. Res. A555 (2005) 36.

[22] H. Dekker et al., The RASNIK-3dimensional alignment system, Proceedings of the 3rd International Workshop on Accelerator Alignment, Annecy, France, 28-30 September 1993, p.147;
H. van der Graaf et al., First system performance experience with the ATLAS high-precision muon drift tube chambers, Nucl. Instr. and Meth. in Phys. Res. A419 (1998) 336.

[23] C. Amelung et al., The ATLAS Muon Alignment System, Proceedings of the first LHC Detector Alignment Workshop, CERN, 4-9 September 2006, Yellow Report.

[24] K. Hashemi and J. Bensinger, The BCAM Camera, ATLAS note ATL-MUON-2000-024, 15.9.2000.

[25] F. Bauer et al., Optical alignment system for the ATLAS muon spectrometer, Proceeding of IEEE Nuclear Science Symposium, Rome (2004).

[26] C. Amelung: ARAMyS - Alignment Reconstruction Software for the ATLAS Muon Spectrometer, Proceedings of the 10th Topical Seminar on Innovative Particle and Radiation Detectors (IPRD 2006), Nuclear Physics B (Proc. Suppl.) 172 (2007) 132-134.

[27] The ATLAS Computing Technical Design Report, CERN-LHCC/2005-022, 20.6.2005, ISBN 92-9083-250-9.

[28] D. Adams et al, Track reconstruction in the ATLAS muon spectrometer with MOORE, ATLAS note ATL-SOFT-2003-007.

[29] P. Branchini et al., Study of drift properties of high pressure drift tubes for the ATLAS muon spectrometer, IEEE Trans. Nucl. Sci. 53-1 (2006) 317;
F. Cerutti et al., Study of the MDT drift properties under different gas conditions, ATLAS-MUON-PUB-2006-004.

[30] R. M. Avramidou, E. N. Gazis, R. Veenhof, Drift properties of the ATLAS MDT chambers, NIM A 568 (2006) 672.